

UNIVERSITY OF THESSALY



***Department of Mechanical and Industrial
Engineering***

***Transport Processes & Process Equipment
Laboratory***

Advanced Master of Science

Serifi Katerina

***HEAT TRANSFER
THROUGH INCLINED
WAVY FILMS***

Supervisor: Professor V. Bontozoglou

June 2004, Volos



ΠΑΝΕΠΙΣΤΗΜΙΟ ΘΕΣΣΑΛΙΑΣ
ΥΠΗΡΕΣΙΑ ΒΙΒΛΙΟΘΗΚΗΣ & ΠΛΗΡΟΦΟΡΗΣΗΣ
ΕΙΔΙΚΗ ΣΥΛΛΟΓΗ «ΓΚΡΙΖΑ ΒΙΒΛΙΟΓΡΑΦΙΑ»

Αριθ. Εισ.: 4022/1
Ημερ. Εισ.: 15-10-2004
Δωρεά: Συγγραφέας
Ταξιθετικός Κωδικός: Δ
621.402 2
ΣΕΡ

“Σε μένα το αίσθημα είναι στην αρχή χωρίς ορισμένο και σαφές αντικείμενο, αυτό σχηματίζεται αργότερα. Προηγείται μια κάποια μουσική διάθεση και έπειτα μου παρουσιάζεται η ποιητική ιδέα.”

Επιστολή του Schiller προς τον Goethe, 18 Μαρτίου 1796

Ευχαριστίες

Η επιτυχημένη ολοκλήρωση μιας δουλειάς στον συγκεκριμένο χώρο και στο δεδομένο επίπεδο (μεταπτυχιακό δίπλωμα ειδίκευσης) είναι συνήθως αποτέλεσμα ιδανικής συνεργασίας.

Κυρίαρχο στοιχείο της παρούσας εργασίας είναι η συνεργασία μου με τον καθηγητή μου Βασίλη Μποντοζογλου. Θέλω να τον ευχαριστήσω θερμά για την πολύπλευρη υποστήριξή του, για την εμπιστοσύνη του, για τα μαθήματα που παρέδωσε είτε κατ' ιδίαν, είτε μέσα στην αίθουσα, ειδικά για το μεταπτυχιακό του μάθημα: Θεωρία ευστάθειας θερμοϋδραυλικών συστημάτων, για το κέφι που ενέπνευσε και το κίνητρο για επιστημονική έρευνα, για την αδιάλειπτη και ουσιαστική παρουσία του στις ώρες της δουλειάς.

Ευχαριστίες οφείλω στα μέλη της τριμελούς μου επιτροπής κ. Μαλαματάρη και κ. Βαλουγεώργη για τις καίριες υποδείξεις τους και παρατηρήσεις. Ξεχωριστά ευχαριστώ τον κ. Μαλαματάρη για τις ώρες που ξόδεψε μαζί μου μαθαίνοντάς μου τον κώδικα που εκείνος είχε δουλέψει.

Ιδιαίτερα ευχαριστώ τον κ. Αράβα και στον κ. Καραμάνο, για τα μεταπτυχιακά τους μαθήματα, η γνώση των οποίων αποτέλεσε βασική προϋπόθεση για την εκπόνηση και ολοκλήρωση της εργασίας .

Ευχαριστώ επίσης τον κ. Πελεκάση και τον κ. Παπαδημητρίου, τόσο για τα μεταπτυχιακά τους μαθήματα όσο και για την διάθεσή τους να συνεισφέρουν όποτε το χρειάστηκα.

Ο κ. Ανδρίτσος είναι μέλος της πενταμελούς εξεταστικής μου επιτροπής. Τον ευχαριστώ ιδιαίτερα.

Βόλος, Μαΐος 2004

ΠΕΡΙΛΗΨΗ

Το φαινόμενο της μεταφοράς θερμότητας από το τοίχωμα στο υγρό που ρέει πάνω από αυτό με τη μορφή λεπτού υμένα βρίσκει πληθώρα εφαρμογών, κυρίως βιομηχανικών αλλά και πιο καθημερινών. Ο συνδυασμός ενδιαφέρουσας ρευστοδυναμικής συμπεριφοράς και πληθώρας εφαρμογών καθιστούν το φαινόμενο αντικείμενο έντονης μελέτης τόσο υπολογιστικής όσο και πειραματικής.

Η υπολογιστική μελέτη της επίδρασης ενός πλήρως διαμορφωμένου και γνωστού ροϊκού πεδίου στη μεταφορά θερμότητας από το τοίχωμα είναι το βασικό αντικείμενο της παρούσας εργασίας. Το ισοζύγιο ενέργειας με κατάλληλες συνοριακές συνθήκες προστέθηκε σε διαθέσιμο κώδικα πεπερασμένων στοιχείων. Φαινόμενα φυσικής συναγωγής αγνοούνται και συνεπώς το ροϊκό πρόβλημα και το πρόβλημα μετάδοσης θερμότητας λύνονται διαδοχικά.

Εξετάζεται λεπτομερώς η επίδραση μίας σειράς μοναχικών κυμάτων στην μεταφορά θερμότητας από το τοίχωμα. Ένα ενδιαφέρον αποτέλεσμα είναι ότι αναπτύσσεται μία στάσιμη κατανομή θερμοροής κατά μήκος του τοιχώματος, που ακολουθεί την κίνηση του κύματος. Μελετάται η επίδραση του αριθμού Peclet στην ένταση της θερμοροής ώστε να διευκρινιστεί η σχετική συνεισφορά των όρων συναγωγής και αγωγής. Για ένα ευρύ φάσμα αριθμών Peclet, η συναγωγή έχει σημαντική συνεισφορά στην κορυφή και την ουρά του μοναχικού κύματος. Η συνεισφορά αυτή, σε συνδυασμό με την λέπτυνση του υποστρώματος μεταξύ διαδοχικών μοναχικών κυμάτων, προκαλεί ενίσχυση της μεταφοράς θερμότητας πέρα από το όριο της καθαρής αγωγής.

ABSTRACT

The phenomenon of heat transfer from a wall to a liquid film which flows along it is encountered not only in industrial applications, but also in every day life. The combination of interesting fundamental fluid mechanics and of numerous applications has made film flow the subject of intense experimental and theoretical/computational study.

The goal of the present work is the computational study of heat transfer from an isothermal wall to a cold film with fully developed flow characteristics. A finite-element numerical scheme is modified with the inclusion of the energy equation and appropriate boundary conditions. Natural convection is ignored and the flow and heat transfer problems are solved consecutively.

The effect of a regular solitary wavetrain on heat transfer characteristics from the wall is investigated. One interesting result is that a stationary periodic flux distribution develops that follows the waves. The effect of Peclet number is studied in order to clarify the relative contributions of conduction and convection to the variation of wall heat transfer. For a wide range of Peclet numbers, convection is found to have a significant influence on the crest and tail of the solitary humps. This effect, in combination with the thinning of the substrate between successive waves, results in heat transfer enhancement above the conduction limit.

Contents

1. Introduction	page 1
2. Theoretical background	3
2.1 Flat film: the flow problem.....	3
2.2 Stability theory of inclined thin sheets.....	5
2.3 Non linear wave evolution on a falling film.....	9
2.4 Heat transfer problem.....	21
3. Problem definition	29
3.1 The flow problem.....	29
3.2 The thermal problem.....	31
3.3 The inflow boundary conditions.....	34
4. Method of solution	39
4.1 Computational domain and solution grid.....	39
4.2 Finite-element discretization of the unknowns.....	41
4.3 The integrally weighted governing equations.....	45
4.4 Space and time integration algorithms.....	47
5. Results and discussion	50
5.1 Heat transfer in flat film.....	50
5.2 Wavy film: The flow field.....	53
5.3 Heat transfer to the wavy film: transient phenomena.....	54
5.4 Wavy film: The thermally quasi-developed flow.....	55
6. Concluding remarks	61
References	62
Appendix	65

Contents of figures

Figure 1. Geometry of film flows.....	page 2
Figure 2. Inclined film flow with waves, physical picture.....	4
Figure 3. The critical Reynolds number R_c as a function of inclination angle.....	8
Figure 4. Schematic of the four waves regimes in a naturally excited evolution on a film flow.....	10
Figure 5. Phase diagram in frequency f and Reynolds number Re showing various regimes of linear stability, nonlinear evolution, and secondary instabilities.....	14
Figure 6. The evolution of solitary waves forced at $f=1.5$ Hz and Reynolds number, $Re=29$	15
Figure 7. The evolution of multi peaked waves forced at $f=4.5$ Hz with Reynolds number, $Re=29$	16
Figure 8. The coalescence two solitary waves.....	18
Figure 9. Downstream evolution of the flow, $fr=1$ Hz.....	19
Figure 10. Wave effect on the heat transfer in fully developed region in a laminar-wavy film (local values) at $T_w = \text{const}$	23
Figure 11. Calculated heat transfer coefficients.....	25
Figure 12. Time averaged heat transfer coefficient.....	27
Figure 13. Variation of heat transfer enhancement with wave frequency.....	28
Figure 14. Sketch of the flow system considered.....	29
Figure 15. Inclined film flow with waves with heated wall.....	32
Figure 16. Differential mass balance in a thin control volume.....	37
Figure 17. Computational domain and finite element' s grid.....	40
Figure 18. The pattern element and the local numeration of the nodes.....	41

<u>Figure 19a.</u> The distribution of the temperature for $Pe=1000$, at four different x-positions.....	51
<u>Figure 19b.</u> The distribution of the temperature for $Pe=200$, at four different x-positions.....	51
<u>Figure 19c.</u> The distribution of the temperature for $Pe=50$, at four different x-position.....	51
<u>Figure 19d.</u> The distribution of the temperature for $Pe=10$, at four different x-positions.....	52
<u>Figure 20.</u> The heat flux from the wall giving from 4 Pe number: 10,50,200,1000.....	52
<u>Figure 21.</u> The formation of a series of a stationary solitary waves.....	53
<u>Figure 22.</u> The heat flux from the wall giving for $Pe=10$ in four consecutive time instants.....	54
<u>Figure 23.</u> The heat flux from the wall giving from 2 Pe number:10,1000 in two different time instants.....	55
<u>Figure 24.</u> The spatial distribution of the wall heat flux for $Pe=50$, at two different time instants separated by 20 dimensionless time units.....	56
<u>Figure 25.</u> The spatial distribution of the wall heat flux for different Pe numbers.....	57
<u>Figure 26.</u> Quasi-steady temperature distribution below the wave for different Pe numbers. (a) $Pe=5$, (b) $Pe=25$, (c) $Pe=50$ and (d) $Pe=200$	59
<u>Figure 27.</u> The mean wall heat flux along one wavelength as a function of Pe number.....	60

1.INTRODUCTION

A film flow is defined as a liquid draining under the effect of gravity, with at least one free boundary. Liquid films have a number of peculiarities. They are, therefore, assigned to a separate class of flows. First of all one should note the small thickness (0.1-1 mm) of the films compared to the characteristic sizes which are usually encountered in nature and patterns of liquid flows. Since typical range of Reynolds numbers is 1-1000, the effect of viscosity forces is almost always essential. On the other hand, the presence of a free surface with scales comparable to the film thickness and to capillary constant means a strong influence of surface perturbations on the film flow. For these reasons the mathematical description of the perturbed motion of a liquid film, even in the simplest statement, is extremely complicated. An essential simplification is, however, possible for long-wave perturbations when the boundary layer approximation seems rather appropriate.

Figure 1 illustrates the typical geometries of several types of film flows. These geometries are encountered in many pieces of industrial equipment, such as heat exchangers, wetted-wall columns, distillation equipment, liquid-liquid extraction towers, evaporators, gas-liquid separators. The gravitational flow of a film over an inclined plane or over the outside surface of a vertical tube has been systematically studied though surfaces of any profile, are encountered in practice, including the rough ones. In particular the cases of film falling down in moving bodies, vibrating and rotating ones, are the most complicated examples. (Alekseenko et al, Wave flow of liquid film,1994)

A combined flow of the liquid film and a gas phase, i.e. two-phase (annular) flow, is frequently realized in engineering. An annular flow is one of the patterns adopted by the vapor-liquid mixture moving in a vapor generating channel. The relative motion of phases results in the

appearance of additional shear and normal stresses at the interface and affects essentially the structure of interface.

In this study, however, attention will be given to the purely gravitational motion of films. To be more specific, the work aims at simulating the heat transfer from the wall to the main mass of fluid. There is urgent interest in the study of the effect of the configuration of a flow field in the heat transfer coefficient, as well as to clarify the mechanism on which this process is based. This means that we want to find out why film flow waves enhance the rate of the heat transfer.

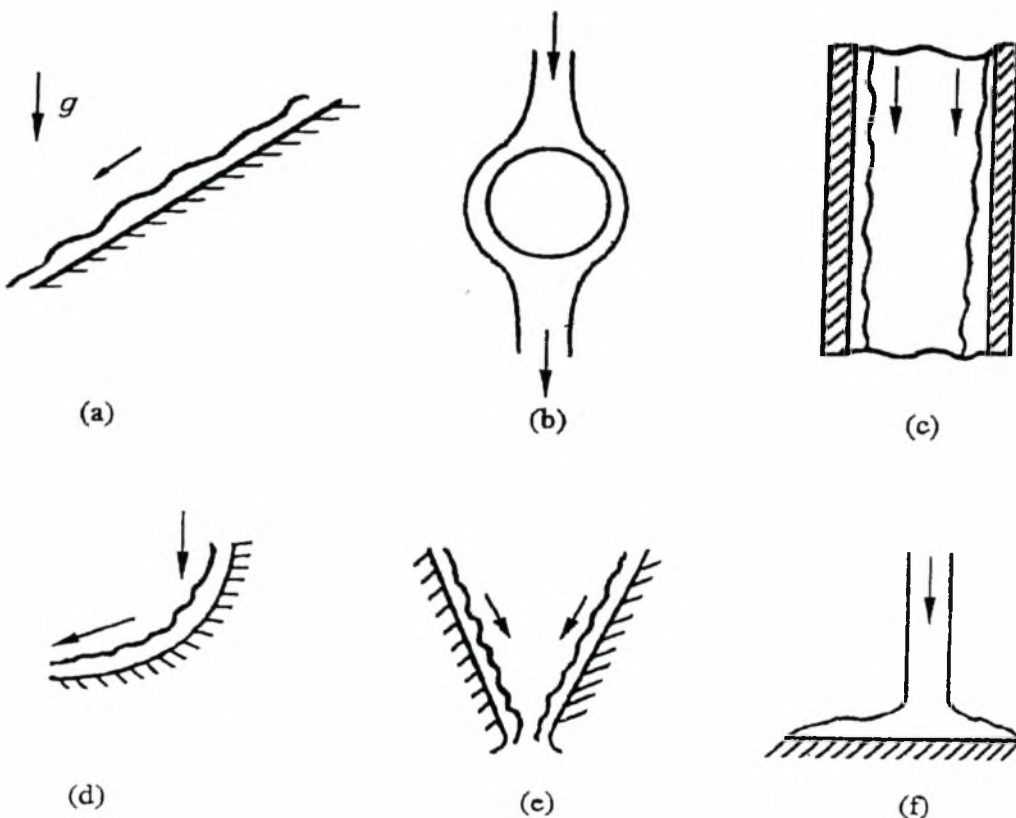


Figure 1. Geometry of film flows: (a) film falling down an inclined surface, (b) flow past a cylinder, (c) film flow along the internal surface of a tube, (d) falling down a curvilinear surface, (e) flow along the internal surface of a cone, (f) jet spreading along the surface

2. THEORETICAL BACKGROUND

In this chapter, the classical falling film theory is reviewed in brief along with modern numerical and experimental studies on the film flow down an inclined wall are presented and discussed.

2.1 Flat film: the flow problem

There have been a number of studies of falling films over the past several decades. One of the earliest of these is that of Nusselt [Nusselt, 1916] dealing with steady laminar flow in a smooth condensate film flowing down a vertical wall under the action of gravity. He obtained the following expressions for the film thickness (h_N), average liquid velocity in the film (U) and the average heat transfer coefficient (λ) in terms of Q , the volumetric liquid flow rate per unit wetted perimeter:

$$h_N = \left[\frac{3\nu}{g} \right]^{1/3} Q^{1/3} = \left[\frac{3\nu^2}{g} \right]^{1/3} \text{Re}^{1/3} \quad (2.1.1)$$

$$U = \left[\frac{g}{3\nu} \right]^{1/3} Q^{2/3} = \left[\frac{\nu g}{3} \right]^{1/3} \text{Re}^{2/3} \quad (2.1.2)$$

$$\lambda = \frac{\kappa}{h_N} \left[\frac{\kappa^3 g}{3\nu} \right]^{1/3} Q^{-1/3} = \left[\frac{\kappa^3 g}{3\nu} \right] \text{Re}^{-1/3} \quad (2.1.3)$$

where g is the acceleration due to gravity, κ the thermal conductivity of the fluid, ν its kinematic viscosity, and Re is the film Reynolds number defined as $\frac{Uh_N}{\nu}$. The above relations are valid for a smooth film.

However, it is well-known that waves form on the surface of the film, even for small liquid flow rates.

The solution that follows is the Nusselt solution for inclined wall. We consider two-dimensional film flow with characteristic length L (Figure 2). The velocity in the x direction does not depend on the length x . We consider constant density and viscosity, as well.

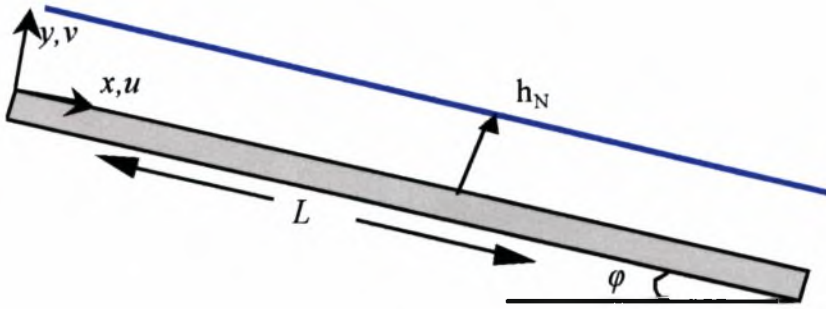


Figure 2. Inclined film flow with waves, physical picture

We consider an elementary volume. The x-momentum enters in that volume by convection with the flow and by the action of viscosity. The balance of x-momentum can be written as follows:

$\left[(dyu)(\rho u) \Big|_x - (dyu)(\rho u) \Big|_{x+L} \right] + \left[L\tau_{yx} \Big|_y - L\tau_{yx} \Big|_{y+dy} \right] + Ly\rho g \sin \varphi = 0$, of unit width, which by dividing dy Ly at the limit $dy \longrightarrow 0$:

$$\frac{d(\tau_{yx})}{dy} + \rho g \sin \varphi = 0 \quad (2.1.4)$$

where: $\tau_{yx} = -\mu \frac{du_x}{dy}$

The boundary conditions are:

$$\left. \begin{array}{l} y=0 \Rightarrow u(0)=0 \\ y=h_N \Rightarrow \tau_{yx}=0 \end{array} \right\} \quad (2.1.5)$$

Solving the equation (2.1.4) subject to the boundary conditions (2.1.5) the following velocity profile is obtained :

$$u(y) = \left(\frac{\rho g h_N^2 \sin \varphi}{2\mu} \right) y(2h_N - y) \quad (2.1.6)$$

The thickness of the film, h_N , is associated to the volumetric flow rate, Q , through the relation:

$$h_N = \sqrt[3]{\frac{3Q\mu}{\rho g \sin \varphi}} \quad (2.1.7)$$

The usual dimensional analysis leads to the Reynolds and Weber numbers or Reynolds and Kapitza ones, which are defined as follows:

$$\text{Re} = \frac{U \cdot h_N}{\nu} = \frac{Q}{\nu}$$

$$\text{We} = \frac{\sigma}{(\rho \cdot U^2 \cdot h_N)}$$

$$\text{Ka} = \frac{\gamma}{(\rho \cdot \nu^{4/3} \cdot g^{1/3})}$$

where: U it is the mean velocity, ρ the density of fluid, σ the surface tension. Several combinations are possible, but we prefer to use the Reynolds number, the inclination angle and a unique Kapitza number that depends only on the physical properties of the fluid and not on the flow rate. The more conventional Weber number can be related to these three parameters.

The mathematic analysis of the general problem of flow with surface waves is nonlinear and difficult enough due to the fact that the shape is unknown and should be introduced as a parameter in the calculations.

2.2 Stability theory of inclined thin sheets

An analysis of the propagation of waves on the surface of a body of water usually leads to a relationship between phase velocity c , liquid depth h , wave amplitude A , wavelength γ , gravity g , and possibly surface tension σ . In the classical linear theory of inviscid water waves, two of the main simplifying assumptions are that the wave amplitude is small compared to the mean depth of the liquid and that the wavelength is large compared to the amplitude. This leads to the dispersion relation

$$c^2 = \left(\frac{g\gamma}{2\pi} \right) \tanh \left(\frac{2\pi h}{\gamma} \right) \quad (2.2.1)$$

for gravity waves. We can see that waves with different wavelengths propagate at different phase velocity, but the amplitude of the wave does not affect the wave velocity, the waves are dispersive but linear.

Thus, if we introduce some kind of disturbance in the inclined film flow, it is well known that this will develop downstream and lead to the appearance of waves. Because of the fact that two-dimensional disturbances are more unstable than three-dimensional ones, the study of linear stability is restricted to two-dimensional disturbances (Squire's theorem). Following the appropriate steps of linear analysis and taking into account the periodicity of the flow, we derive a fourth-order linear homogeneous ordinary differential equation for the amplitude, f , of the streamfunction $\Psi = f \exp[i\delta(x - ct)]$, where δ is the wavenumber and c is the phase velocity.

The equation, derived independently by Orr and Sommerfeld, is

$$f'''' - 2\gamma f'' + \gamma^4 f = i \frac{\gamma}{v} \left[(u - c)(f'' - \gamma^2 f) - u'' f \right] \quad (2.2.2)$$

where $c = \frac{\omega}{\gamma}$ is the complex phase velocity, ω is a complex constant called complex growth rate or complex cyclic frequency. Nondimensionalizing all variables using L as characteristic length, U as characteristic velocity, and L/U as characteristic time, we recast the Orr-Sommerfeld equation into the dimensionless form

$$\hat{f}'''' - 2\delta^2 \hat{f}'' + \delta^4 \hat{f} = i \text{Re} \delta [(\hat{U} - \hat{c})(\hat{f}'' - \delta^2 \hat{f}) - \hat{U}'' \hat{f}] \quad (2.2.3)$$

where we have defined the following dimensionless variables and constants $\hat{f} = \frac{f}{UL}$, $\hat{U} = \frac{u}{U}$, $\hat{c} = \frac{c}{U}$, $\hat{x} = \frac{x}{L}$, $A = \delta L$, $\text{Re} = \frac{UL}{v}$

The primes indicate differentiations with respect to the dimensionless position vector \hat{x} .

In the temporal stability problem we specify the real wave number k and supply proper boundary conditions for f to obtain an eigenvalue

problem for c . The boundary conditions of inclined film flow problem are:

1. Non-slip and no-penetration condition on the solid wall :

$$\text{At } y=0, \quad u = v = 0 \rightarrow f(0) = f'(0) = 0$$

2. Balance of forces on the free surface: $\left(\begin{matrix} \tau \cdot n \\ - \\ - \end{matrix} \right) \cdot t = 0$ and $\left(\begin{matrix} \tau \cdot n \\ - \\ - \end{matrix} \right) \cdot n = \sigma \eta$,

where η is the curvature.

The real part of c is the phase velocity of the perturbation. Having obtained c , we compute the complex growth rate $\tau = \delta c$ and decompose it into its real and imaginary parts $\tau = \tau_R + i\tau_I$ to obtain the growth rate of the perturbation τ_I . At neutral stability $\tau_I = 0$ and both c and τ are real. In dimensionless variables, the solution of the temporal stability problem depends upon the magnitude of the Reynolds number Re and dimensionless wave number δ .

If the imposed disturbance ($e^{i\delta(x-ct)}$) has wavelength much larger than the film thickness and if we consider a regular perturbation expansion (Yih, 1963), then from the zero order solution we obtain $c_0 = 3$. This means that the first wave which appear have infinite wavelength and the phase velocity of its motion is three times faster than the mean film velocity.

From the first order solution, we reach the conclusion that there exists a critical Reynolds number Re_c below which the flow is stable for all wave numbers: $Re_c = \frac{6}{5} \cot \varphi$. This relation of critical Reynolds number with the angle of inclined wall was confirmed experimentally by Liu et al. (1993). Figure 3 illustrates the critical Re related to the angle for two different fluids (Liu et al, 1993). The data are compared with the theoretical prediction $Re_c = \frac{6}{5} \cot \varphi$, given by the solid line. The agreement is quite satisfactory, and this implies that physical

approximations made in the formulation of the stability theory are correct at least near the critical point.

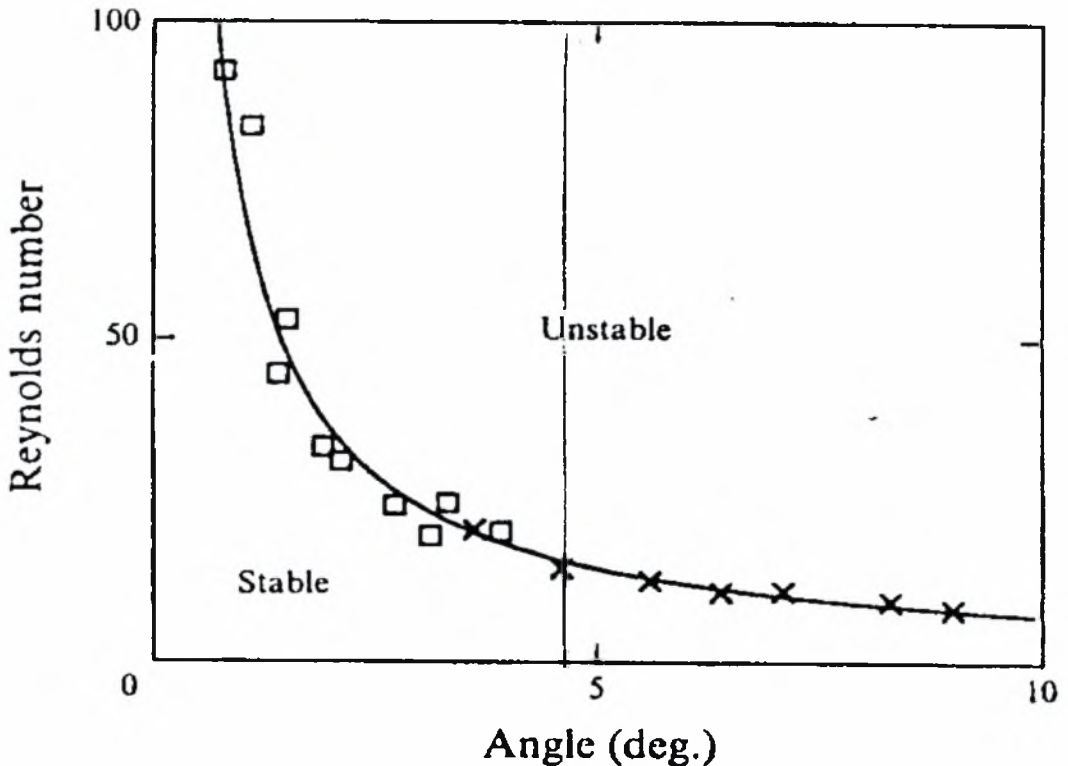


Figure 3. The critical Reynolds number R_c as a function of inclination angle. Results from both water (\square) and glycerin-water solutions (\times) are shown. The solid line is $Re_c = \frac{6}{5} \cot \varphi$.

The experimental measurements were taken with water and solution of water- glycerin 26%. The two lines of data coincide proving that the instability depends only on the Reynolds number and the kind of the fluid does not affect it .

In the spatial stability problem we set $\delta = \delta_R + i\delta_I$, where δ_R is the real number of the perturbation and $-\delta_I$ is the corresponding spatial growth rate, and $\tau = \tau_R$, where τ_R is the real cyclic frequency of the perturbation. We then specify τ_R and supply proper boundary conditions for f to obtain an eigenvalue problem for δ_R and δ_I . At neutral stability

$\delta_i=0$ and δ is real. In dimensionless variables, the solution of the spatial stability problem depends upon the magnitudes of the Reynolds number Re and dimensionless real cyclic frequency, ω , of the flow. (Pozrikidis, Introduction to theoretical and computational fluid dynamics, 1997)

2.3 Non linear wave evolution on a falling film

The downstream evolution of film flow along an inclined wall can be categorized depending on the Reynolds number. Thus, at very large Reynolds numbers ($Re>1000$), the waves observed on the film flow are of the shear-wave variety with wavelengths comparable to or shorter than Nusselt film thickness h_N . Such high-flow-rate conditions typically yield turbulent films (turbulent in the classical sense) dominated by internal Tollmien-Schlichting disturbances. The interfacial dynamics is simply enslaved by the internal turbulence. At moderately high Reynolds numbers ($300<Re<1000$), long interfacial waves characteristic of gravity-capillary instabilities begin to appear (Chu & Dukler 1974). However, the wave dynamics is extremely nonstationary, especially for the persisting short waves which seem to be generated by a vortex shedding mechanism from the long waves. At extremely low flow rates ($Re\ll 1$), the film becomes so thin that intermolecular forces and contact line dynamics become important as the film ruptures. In the intermediate region ($1<Re<300$) the instability consists of long interfacial waves dominated by gravity-capillary effects. Among others Chang (1994) has recognized four distinct regions in the development of inclined film flow (Figure 4).

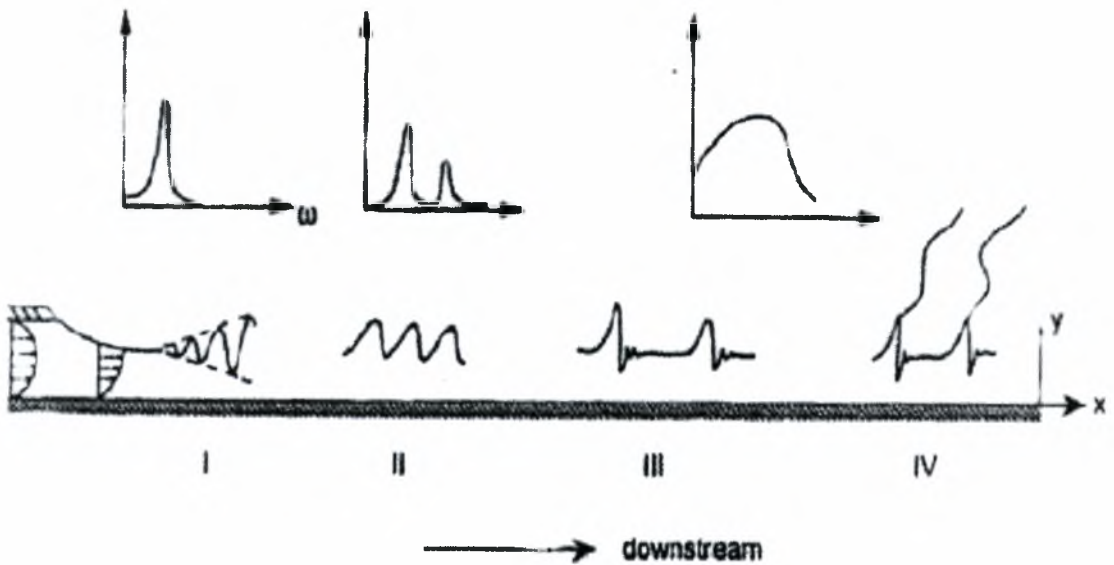


Figure 4. Schematic of the four waves regimes in a naturally excited evolution on a film flow. The wave spectra from localized probes at the four regions are also shown. The parameter ω is the wave frequency. For higher Re values ($R > 50$), region III may not be present.

In the inception region (region I), infinitesimal disturbances at the inlet are amplified downstream to form a monochromatic wave at the end of the region, indicating that the instability is a convective one and not of the absolute variety. If the initial disturbance is sufficiently monochromatic in frequency, the emerging wave inherits the forcing frequency. If the disturbance has a wide band of frequency, as is true with natural noise, a highly selective linear filtering process in region I yields a unique monochromatic wave field for all wide-band disturbances. In particular, transverse disturbances are selectively damped in this inception region. Within this region, the amplitude of the monochromatic wave grows exponentially downstream as in all linear excitation processes of convectively unstable systems. Beginning in region II, however, the exponential growth is arrested by weakly nonlinear effects as the amplitude of the monochromatic wave saturates to a finite value dependent on the wave number, Reynolds number and

Kapitza number. Due to this weakly nonlinear interaction between an unstable fundamental Fourier mode and a stable second harmonic, the monochromatic wave of region I begins to develop a finite overtone in region II as its sinusoidal shape steepens downstream. There is also a negative nonlinear correction to the wave speed of the inception region such that the waves actually slow down as they grow (Lin 1983). Some experimental evidence indicates that even the wave number of the saturated periodic wave exiting from region II, which is still a very uniform wave field, is different from that of the monochromatic wave emerging from region I due to a nonlinear selection mechanism. In periodically forced experiment with sufficiently large forcing amplitude, both region I and region II may be bypassed and the first uniform wave field that emerges contains large-amplitude waves whose wave frequencies are close to the forcing frequency except at very low values (Kapitza & Kapitza 1949, Alekseenko et al 1985). The periodic finite-amplitude disturbances in a forced experiment can hence entrain waves that would not have been selected by the linear and nonlinear selection mechanisms of region I and II. For small-amplitude and broad-banded natural or artificially introduced disturbances, however, the uniform wave fields emerging from regions I and II are independent of the disturbances present. They are uniquely selected by the linear and nonlinear mechanisms in region I and II.

Both finite-amplitude wave fields generated by periodic forcing and naturally excited wave fields emerging from region II travel a long distance (~ 10 wavelengths) in a stationary manner, e.g. without visible changes in their shape or speed, before they undergo another slow evolution in region III. Here, two dominant instabilities of the finite-amplitude waves have been observed. The best data are recorded by Liu & Gollub (1994) for inclined films. Neighboring waves coalesce at intermittent locations due to a subharmonic instability (Prokopiou et al 1991) or long-wave modulation appears characteristic of sideband

instabilities (Cheng & Chang 1992a). These two instabilities create intermittent patches of defects to the otherwise uniform field of waves. Within these patches, the distorted waves grow in wavelength, amplitude and speed and evolve into characteristic spatially localized teardrop humps. These humps have steep fronts which are relaxed by a series of front-running bow waves whose wavelength is close to the monochromatic waves at inception. These larger and faster humps begin to expand the patches in the downstream direction as they overtake the original slower waves, so much so that all of latter may vanish eventually. The wave frequency or wave number spectrum now becomes very broad, in contrast to the monochromatic spectrum in region I and the fundamental-overtone pair in region II. This, however, does not imply that continuous band of dispersive waves dominate the interface as in turbulent channel flow. Instead, a large portion of the band is locked into the characteristic hump of the evolved waves and travels in synchrony. The broad-banded spectrum is due mostly to the localized shape of the humps which is strikingly identical. These robust humps have a characteristic length that is much shorter than the typical separation between humps where the film is essentially flat. They are hence referred to as solitary waves, or solitary humps. The separation between the individual humps are typically nonuniform and time-varying, indicating nonstationary interaction among them and reflecting the spatio-temporal irregularity of their births. However, the humps themselves remain nearly identical and do not alter their shape significantly during the interaction within region III.

Finally, in region IV, transverse variation begins to develop on the wave crests of the solitary humps. The dynamics of the transverse variation is nonstationary and these transverse variations grow to such amplitude (not in height but in the direction parallel to the wall) that adjacent crests merge at various points and pinch off. However, the wave shape in the flow direction (x in Figure 4) retains the solitary

shape except near the pinch points. For vertical water films at low Reynolds numbers, regions I and III occupy 30 to 40 inception wavelengths with each region spanning about 10 wavelengths. (The wavelength selected at inception is about 1 cm for water at the Reynolds number of interest.) Region IV seems to persist indefinitely downstream. If the introduced disturbance at the feed, or elsewhere in the channel, contains significant transverse variation such that it is not entirely filtered in the inception region I, then region III may be negligible in length or may be skipped entirely.

The former have been confirmed experimentally by Liu and Gollub (1994). To provide a comprehensive view of their work we show in Figure 5 a phase diagram in frequency and Reynolds number that pulls together interesting experimental results.

The circles are measurements of the neutral stability frequency f_c , below which the free surface is unstable. The upper solid line is calculated from linear stability theory. The triangles show measurements of the maximum amplified frequency f_m , and the solid line through them is also the result of linear theory. We see that the linear stability theory is quite successful.

The bifurcation phase boundary denoted f_s separating two types of nonlinear evolution is given by the diamonds in Figure 5, with a smooth dashed line drawn through them. Between f_s and f_c we find saturated finite-amplitude waves with one maximum per period. Below f_s , waves evolve into multi-peaked waveforms, including solitary waves, by strongly nonlinear mechanisms.

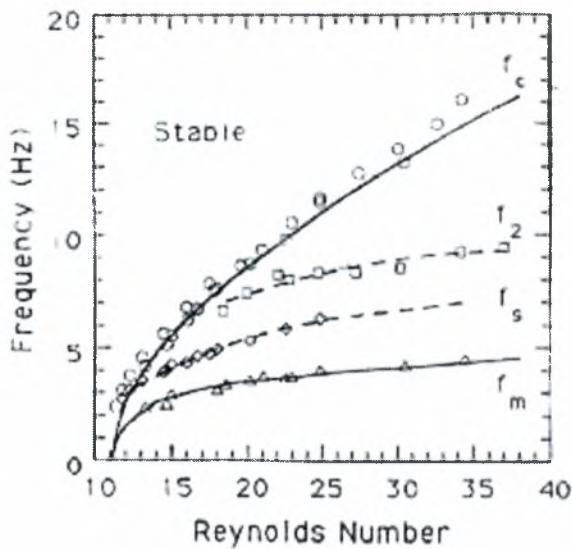


Figure 5. Phase diagram in frequency f and Reynolds number Re showing various regimes of linear stability, nonlinear evolution, and secondary instabilities. The inclination angle is $\varphi = 6.4^\circ$, and the aqueous solutions of glycerin is 54% by weight .

Secondary instabilities: Another phase boundary f_2 shown by squares separates the sideband and subharmonic two-dimensional secondary instabilities of periodic waves. The sideband instability of the primary waves predominates above f_2 , and the subharmonic instability at frequencies below the boundary [and close to f_m]. These secondary instabilities are convective and hence sensitive to noise.

An example of nonlinear periodic wave (solitary wave) evolution is given in Figure 6, where the forcing frequency is 1.5 Hz (Liu & Gollub, 1994). Three wave profiles are taken at increasing distances from the source to show the spatial evolution. Initial sinusoidal waves near the inlet (not shown) become separated, developing steep fronts and stretched tails as the waves move downstream. Subsidiary wave fronts nucleate while primary peaks grow larger [Figure 6 (a)]. Further downstream, the primary waves gradually saturate [Figure 6 (b)]. Eventually, the solitary waves reach a stationary state in which successive pulses are nearly identical [Figure 6 (c)]. The generation of

subsidiary waves may be viewed as a buckling of the surface as it is compressed by rapidly moving solitary humps. When the frequency becomes larger, the primary wavefronts are closer together and the solitary waves cannot be clearly separated. The significant overlap of the front and tail may lead to strong interactions of these approximate solitary waves.

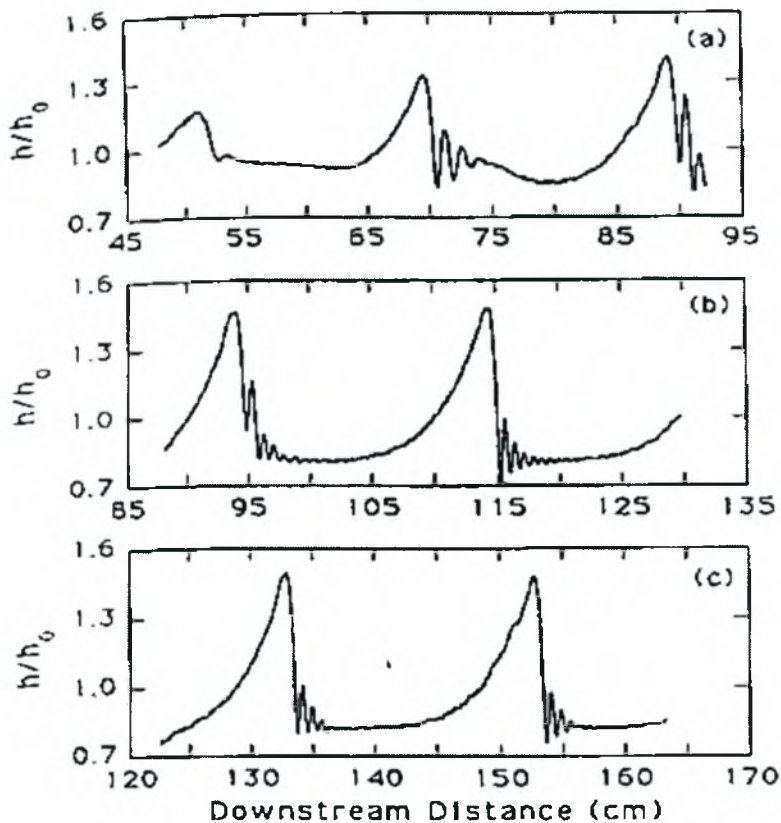


Figure 6. The evolution of solitary waves forced at $f=1.5$ Hz and Reynolds number, $Re=29$.

As the frequency is increased further in the multi-peaked wave regime, the interactions become very pronounced and separate pulses are not formed. An example is shown in Figure 7 for a wave at $f=4.5$ Hz. When the subsidiary wave front is initially generated, a small depression appears on the primary peak and moves faster [Figure 7 (a)]. The velocity of a small depression is about 25.4 cm/s while the primary wave travels at 23.8 cm/s . The small depression passes the

primary peak, and appears to form a subsidiary peak of that primary wavefront [Figure 7 (b),(c)]. It is worth mentioning here that the waves are always periodic in time before losing their stability, even though they may appear nonperiodic in space (Liu & Gollub, 1994).

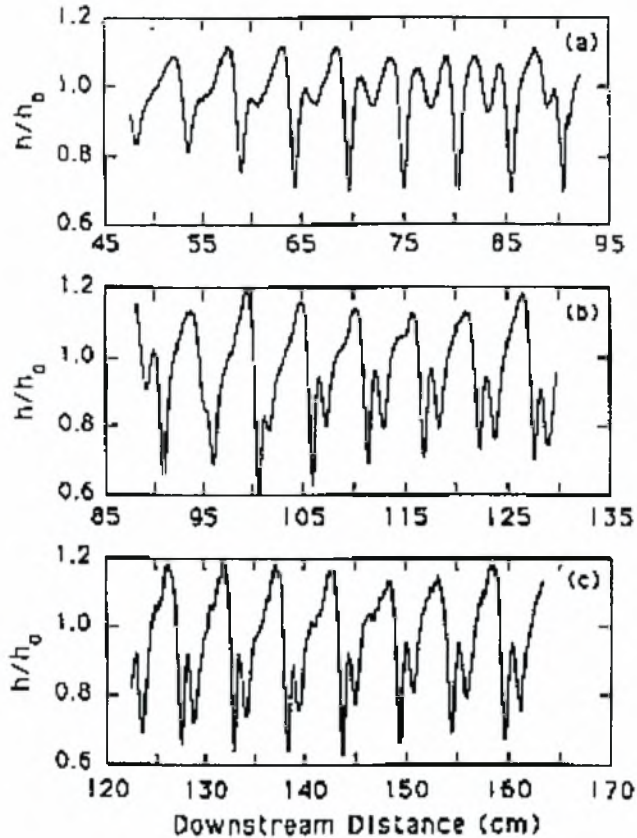


Figure 7. The evolution of multipeaked waves forced at $f=4.5$ Hz with Reynolds number, $Re=29$

The experimental results of Liu & Gollub have been expanded recently by Vlachogiannis & Bontozoglou (2001), who investigated experimentally the interactions between solitary waves. They have systematically observed a large number of coalescence events and recorded their detailed characteristics. The time duration of the merging process was found to be inversely proportional to the height difference of the interacting humps, supporting the conclusion that humps of similar size do not coalesce but may form double-hump structures. They

have witnessed the temporary recession of the front-running ripples and the formation of the an elevated back-substrate. The size of the substrate was found to scale with the height of the wave, and its decay with time was found to obey an exponential law. Measurements of the characteristics and evolution of the elevated back-substrate provide the first experimental confirmation of the predictions of Chang et al.(1995).

In most experiments with water, the elevated substrate yielded to an instability producing an oscillatory tail. This tail was observed to lag behind as isolated hump and eventually decay. On the contrary, if the excited hump was followed closely by another solitary wave, the tail might be trapped in between and result in the nucleation of a new hump. This tail modulation appears not to have been previously noted in the falling-film literature, though it has long been known as an adjustment mechanism of inviscid solitons of the Korteweg-de Vries equation.

A qualitative description of wave-wave interactions and of the decay of excited solitary humps may be accomplished in terms of simple mass conversation arguments. Extending the mechanicm described by Chang et al (1995), Vlachogiannis & Bontozoglou (2001) view both the elevated back substrate and the outcome of its instability, the tail modulation, as effective means of draining liquid from the back of the tail. These mechanisms operate in parallel with the front-running ripples, which stabilize all solitary humps (normal or excited) by draining liquid out from the crest. A coalescence event is recorded in Figure 8.

In view of the above, a key parameter of wave-wave interaction seems to be the degree of excitation of the preceding wave, as represented by the elevation of its back substrate or the intensity of its tail oscillation. In particular, when the preceding wave is not excited it may be approached by a larger (i.e. faster) following wave. Then, the liquid draining out from the front of the second solitary wave raises the

substrate between the two crests leading to the formation of a single hump.

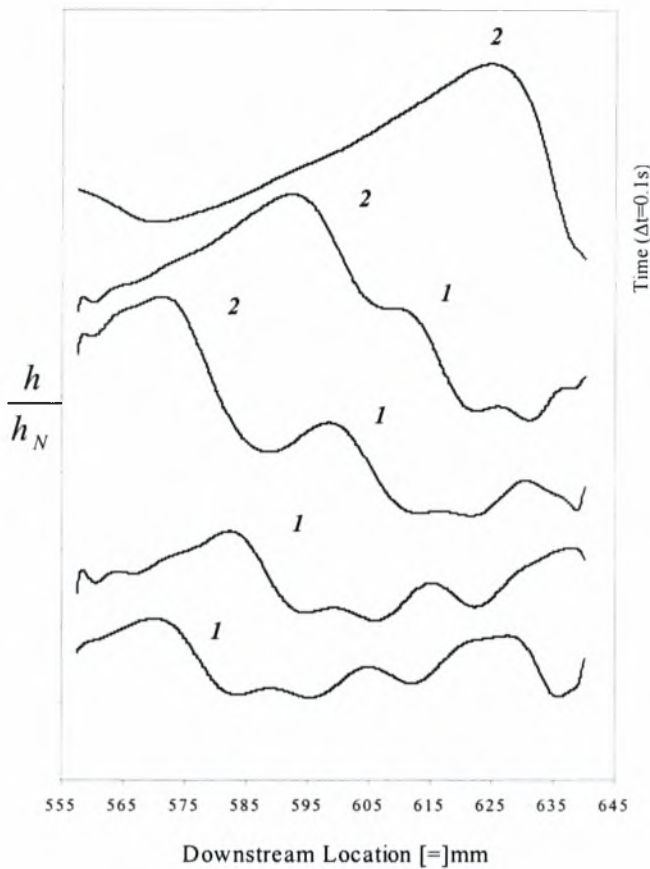


Figure 8. The coalescence of two solitary waves



On the contrary, a preceding excited wave resists coalescence with a bigger hump approaching from behind. If the difference in height is small, the two crests do not approach very closely. Liquid released from the tail of the preceding excited wave is then augmented by liquid drained from the front of the following wave and nucleation of a new hump between the interacting waves may occur. Even when the following wave is much larger and sweeps the distance towards the first hump, it may be decelerated by the liquid draining from the tail of the

excited preceding wave. The resulting structure then involves a quasi-stationary two-humps pulse.

Malamataris, Vlachogiannis, and Bontozoglou (2001) compared the above experimental results with simulations. Based on these simulations, the picture of solitary hump interaction seems to agree with the (relatively limited) experimental information.

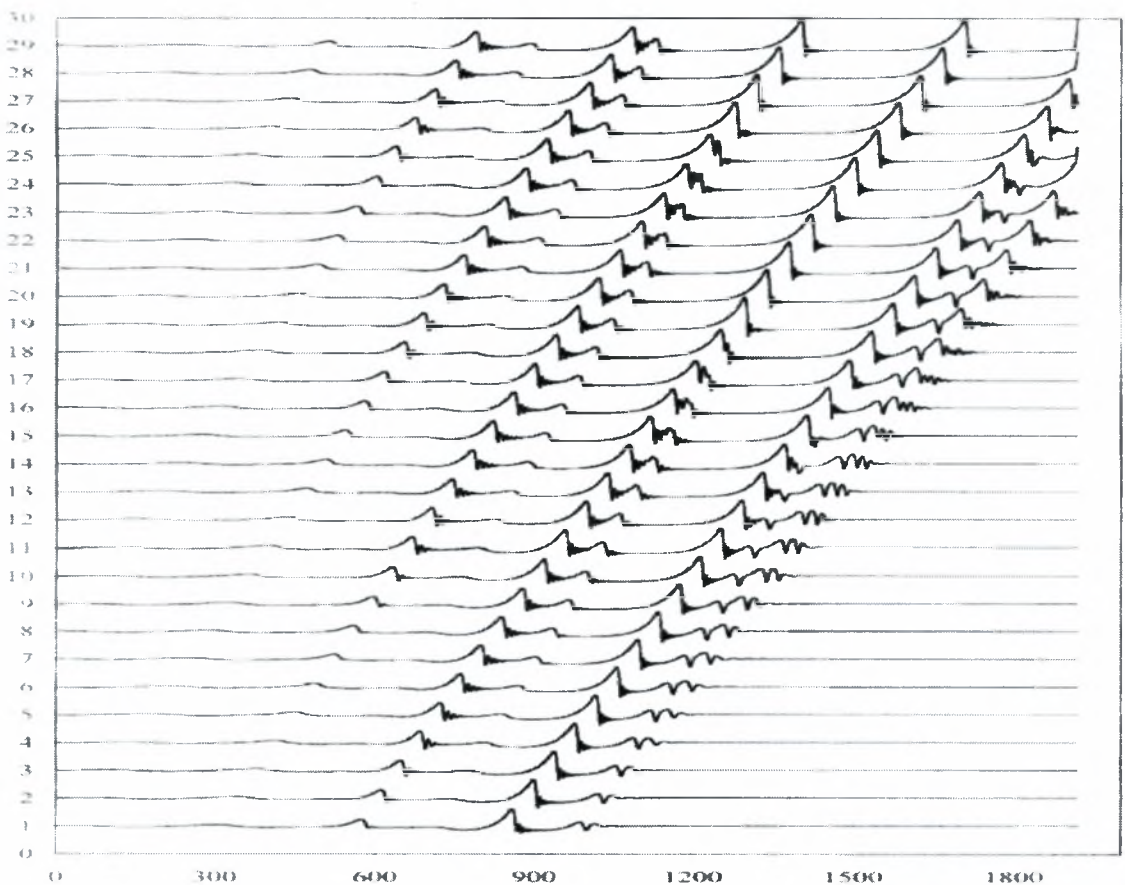


Figure 9. Downstream evolution of the flow for initial disturbance 1 Hz. We can notice the coalescence of solitary humps.

Ramaswamy et al (1996), carried out numerical simulations in order to study interfacial instabilities in thin-film flow. They develop an extensive numerical scheme based on the direct solution of the Navier-Stokes equations. In concurrence with what is known about thin-film instability based on linear and approximate non-linear theories, finite-amplitude waveforms are the stable solution for wavenumbers smaller than the linear critical wavenumber. For wavenumbers close to critical,

the waveforms are nearly sinusoidal. For wavenumbers much smaller than critical, the wave forms are solitary. This transition from nearly sinusoidal waveforms to solitary seem to pass through a quasi-steady regime, in which the spatial harmonic coefficients are in a state of constant fluctuations. Comparison between the full-scale computations and approximate nonlinear theories indicates that these theories are accurate in the parametric regimes for which they are derived. Since only a very small number of comparisons have been made it was not possible to derive definite boundaries delineating the regimes where the approximate nonlinear theories are accurate. Both the Reynolds number and the surface tension influence the accuracy of the approximate nonlinear theories. In the event of large wave amplitude and/or wave steepening, none of the approximate nonlinear theories can be used, and experiments or full-scale computations based on the solution of the complete Navier-Stokes equations will need to be used. The spatial stability analysis of the thin-film instability has been studied by considering a very long domain with periodic forcing at the inlet and absorbing boundary conditions at the exit. Very good agreement with the experiments of Liu & Gollub (1994) has been obtained. Depending on the frequency of excitation, the waves formed downstream are either nearly sinusoidal or solitary or quasi-periodic. Owing to the amplitude dependence of the wave speed, complex wave interactions are likely to occur on the gas-liquid interface. Waves with larger amplitude travel faster and coalesce with smaller waves. This wave interaction is found to be completely inelastic and the resultant wave grows further in amplitude and travels downstream leaving behind a nearly flat interface. However, there appears to be a natural wavelength that the system tries to achieve in the solitary wave regime. The resultant wavelength downstream is also weakly dependent on the initial condition. A powerful numerical technique has been developed and applied to the study of surface wave instability on thin-film flow.

2.4 Heat transfer problem

The dynamics of the free surface significantly affect the heat transfer between the wall and the falling liquid film. The heat transfer from the free surface itself is less significant. It has actually been shown (Gimbutis,1988) that the heat transfer through the free surface can be neglected if $q_{TS} / q_{TW} \leq 0.15$, where q_{TS} is the heat flux at the interface and q_{TW} is the specific heat flux at the wall.

Nusselt (1916) was the first to perform the theoretical analysis of heat transfer from the wall for laminar liquid film under the boundary conditions $T_w = \text{const}$ and $q_{TS} = 0$. He has calculated the heat transfer in both thermally developing and fully developed regions, which is described by the following expressions for the local heat transfer coefficient λ and local Nusselt number Nu^* :

$$\lambda = -\kappa \left. \frac{\partial T}{\partial y} \right|_{y=0} / (T_w - T_f) = 1.88\kappa / h_N \quad (2.4.1)$$

$$Nu^* = \frac{\lambda h_N}{\kappa} = 1.88 \quad (2.4.2)$$

Here T_f is the temperature averaged over the mass flow rate in the given section of the film, κ is thermal conductivity, $W/(m \cdot K)$, h_N is thickness of liquid film.

The heat transfer in a fully developed smooth laminar film is well described by the formula (2.4.2) The solutions (Limberg, 1973; Sobin, 1980; Gimbutis, 1988) which are more rigorous as compared with the Nusselt calculation, are obtained for a thermal inlet region. Since the Prandtl numbers, ($Pr = \frac{\nu}{\alpha}$, ν is the kinematic viscosity and α is the thermal diffusivity) are usually large, then the development of the thermal boundary layers takes place at the background of a hydrodynamically fully developed flow. Therefore the heat transfer problem in the film becomes equivalent to the problem by Graetz (1885) concerning the heat transfer in a plane slot with two-sided heating or

cooling. But this case has been studied in detail in the literature (Zhukauskas & Zhyugzhda,1969). For practical purposes Gimbutis (1988) recommends the following generalized equations for local Nusselt number which generalize quite well the experimental data in the case of the laminar flow of smooth films

$$Nu^* = \frac{15}{8} \left[1 + 0.00072(16Pe \frac{h_N}{x})^{4/3} \right]^{1/4} \quad (2.4.3)$$

at $T_w = \text{const}$,

$$Nu^* = 2.06 \left[1 + 0.0011(16Pe \frac{h_N}{x})^{4/3} \right]^{1/4} \quad (2.4.4)$$

at $q_{TW} = \text{const}$.

where Pe is the Peclet number.

When $x \rightarrow \infty$ from equation (2.4.4) we obtain the known expression for fully developed heat transfer at $q_{TW} = \text{const}$: $Nu^* = 2.06$

The mean heat transfer was studied in most experimental works (Bays, McAdams, 1937; Sexauer,1939; Chernobytsky & Vorontsov,1968; Vorontsov & Tananaiko, 1972). The derivation of empirical formulae for the calculation of the average heat transfer coefficient depending on the flow conditions is presented in the book by Tananaiko & Vorontsov (1975).

The most interesting experimental data on local heat transfer were obtained by Wilky (1962) and Gimbutis (1988). It has been noted that the wave effect is virtually absent at the inlet region that agrees with mass transfer data and it is accounted for by a slight penetration of perturbations into the wall neighborhood where the thermal boundary layers develops. Wilke (1962) was the first to discover the wave effect on the heat transfer. He has shown that a noticeable augmentation of heat transfer from the wall to a laminar wavy film occurs only in the fully developed zone at rather large Prandtl numbers attaining 100%, for example, at $Pr=104$ and $Re \approx 150$. These results are presented in Figure 10. Wilke has accounted for the wave effect by the presence of

additional convective heat transfer and he has introduced the notion of wave thermal diffusivity for its quantitative account. Then the heat flux will be written in the most general form as:

$$q_T = -C_p \rho (\alpha + \alpha_w + \alpha_t) \frac{dT}{dy} \quad (2.4.5)$$

where $\alpha, \alpha_w, \alpha_t$ are the molecular, wave and turbulent thermal diffusivity coefficients, respectively, C_p is the specific heat, $J/(kg \cdot K)$ and ρ the density.

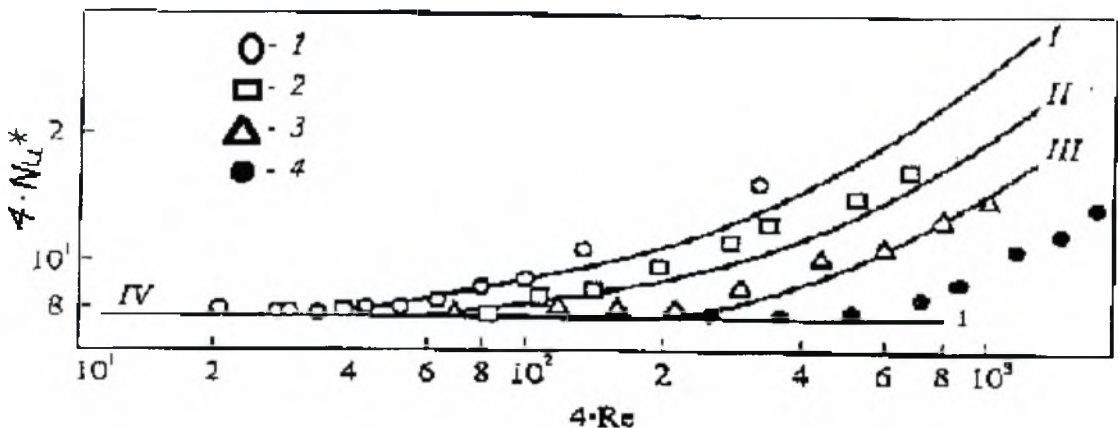


Figure 10. Wave effect on the heat transfer in fully developed region in a laminar-wavy film (local values) at $T_w = \text{const}$. Experiment by Wilke (1962): 1-Pr=210, 2-Pr=104, 3-Pr=43, 4-Pr=9.4. Calculations by Gimbutis (1988) with allowance for waves : I-Pr=210, II-Pr=104, III-Pr=42, IV-formula (2.4.2)

Gimbutis (1988) has developed a technique for calculating the coefficient α_w using the empirical data. In this scheme it is sufficient to know the wave parameters without information on the surface structure. As a result calculation formulae were obtained, whose predictions are shown in Figure 10 in comparison to experimental data by Wilke (1962).

Jayanti and Hewitt (1995) studied the hydrodynamics and heat transfer of wavy thin film flow using computational fluid dynamics techniques. They investigated the effect of sinusoidal and solitary

waves on the heat transfer across the film. Three types of wave shapes commonly found in falling films were included in the study, and the emphasis was on the role of the interfacial waves on heat transfer across the film. In as much as the wavy flow hydrodynamics are not defined entirely by the mean film thickness (wave parameters such as amplitude, shape and wavelength also affecting the mean flow velocity), the concept of equivalent Reynolds number has been proposed as the basis for comparing a smooth film and a wavy film: The heat transfer enhancement in wavy film flow is determined by comparing its heat transfer coefficient with that expected (from Nusselt's theory) in a smooth film having the same film Reynolds number. The calculations were performed for steady state, and no account was taken for any evolution of the shape of the wavy film either with distance or time. The underlining assumption is that any time-dependent evolution of the wave shape is slow enough so that the hydrodynamics are not severely affected by it.

The calculations by Jayanti and Hewitt (1995) have shown that for small-amplitude sinusoidal waves, there is no recirculation under the wave crests, and that the mean flow velocity is not much different from that of a smooth film of the same mean film thickness. In the case of large-amplitude sinusoidal wave, the mean flow velocity, and thus the Reynolds number of the flow, increase for the same mean film thickness. Although the heat transfer coefficient still corresponds to that given by the local film thickness, this decrease in the effective film thickness gives rise to an enhancement in the heat transfer coefficient. In the case of solitary waves, their large amplitude has two consequences: firstly, a large recirculation zone develops under these waves, and secondly, since the flow cross-sectional area is much higher under the wave than in the substrate, the mean velocity and the recirculation velocity are small. The contribution of recirculation to heat transfer rate is small, and the overall heat transfer coefficient is still

dominated by the conduction process through the inter-wave substrate region. Since most of the fluid is transported in these large waves, the substrate film is thinner and the effective heat transfer coefficient therefore higher. The effect of waves on heat transfer in thin films is therefore an indirect one, and is due to the effective thinning of the film rather than to enhanced convection within the waves. The table below summarize the overall effect of convection in the heat transfer coefficient by calculating the average heat transfer coefficient in the wave and comparing it with that obtained due to conduction alone, for three cases corresponds to: $\frac{\lambda_p}{\lambda_s}=2$, $\frac{\lambda_p}{\lambda_s}=4$ and $\frac{\lambda_p}{\lambda_s}=6$, where λ_p is the peak height of the wave and λ_s the substrate thickness.

Case	λ under wave only [W m ⁻² K ⁻¹]			λ under wave and substrate [W m ⁻² K ⁻¹]		
	calculated	theory (conduction)	calc/theory	calculated	theory (conduction)	calc/theory
1	4.912	4.916	0.999	6.109	6.108	1.000
2	3.537	3.471	1.019	5.540	5.507	1.006
3	3.145	2.829	1.111	5.378	5.241	1.026

Figure 11. Heat transfer coefficients in the solitary wave calculations

When averaged over the wave region only, there is virtually no enhancement due to convection in the first case while it is more than 10% in the third case. When considered over the wave and the substrate film, the recirculation-induced enhancement is very small, of the order of a few per cent, even in the third case. This shows that the overall heat transfer rate in thin film flow is not improved significantly by recirculation under the waves. (Jayanti & Hewitt, 1995)

Miyara et al (1995), Miyara et al (1999), Miyara et al (2001), Miyara et al (2002) carried out extensive simulations, in order to study the effect of waves occurring on a falling condensate film (vertical wall) on heat transfer. They investigate the relation between the film flow dynamics and the heat transfer coefficient and partly confirm the results of Hewitt (1995). The enhancement of heat transfer is attributed mainly

to the decreasing time average film thickness due to waves, and the disturbance effects of the waves are small. Miyara verifies that a small amplitude disturbance generated as inflow boundary develops to a solitary wave which consists of a large amplitude hump and small amplitude capillary waves. A circulation flow occurs in the hump that affects temperature distributions, especially for high Prandtl number liquids (low thermal diffusivity). More specifically, the heat transfer enhancement mechanisms by the interfacial waves have been clarified by showing the temperature fields for different Prandtl number liquids. The interfacial waves enhance the heat transfer by two kinds of effects which are the film thinning effect and the convection effect. For low Prandtl number, the convection effect may be neglected and for high Prandtl number both the effects are dominant. Spatial distributions of the time averaged heat transfer coefficient at the wall surface are shown in Figure 12 for different Prandtl number. The time averaged dimensionless heat transfer coefficient (heat flux) is calculated from the time averaged temperature gradient at the wall, as follows:

$$\bar{\lambda} = \frac{\bar{\lambda}' h_0'}{\kappa} = \frac{\partial \bar{T}}{\partial y} \Big|_{y=0}$$

where $\bar{\lambda}'$ is the dimensional heat transfer coefficient and κ is thermal conductivity of the liquid. The time-averaged reciprocal of the film thickness \bar{h}^{-1} represents the heat transfer coefficient for the case of the linear temperature distribution, which corresponds to that for $Pr \rightarrow 0$ and indicates the heat transfer enhancement rate by the local film thinning. $\bar{\lambda}$ includes both the effects of the film thinning and the circulation zone. In the fully developed region, $x > 200$, $\bar{\lambda}$ increases with increase of Prandtl number.

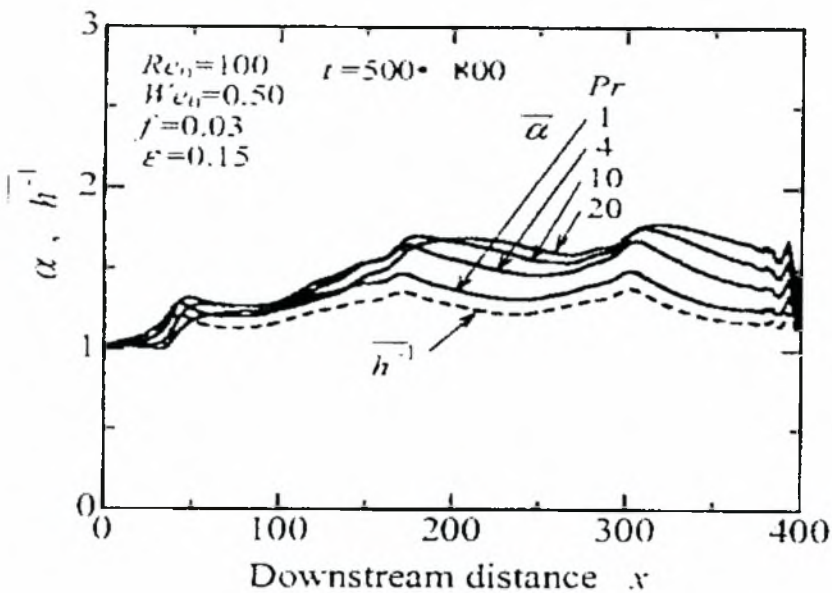


Figure 12. Time averaged heat transfer coefficient

The time averaged heat transfer coefficient increases downstream. In the fully-developed region of the waves, the heat transfer coefficient at higher Prandtl numbers also increases. In the developing region, however, the higher Prandtl number liquid has the lowest heat transfer coefficient (Miyara 1999). Recently, Miyara (2002) has studied numerically and experimentally the effect of wave frequency on heat transfer enhancement. The enhancement rates depend on wave frequency and have a maximum at a certain frequency. Figure 13 shows the variations of the heat transfer coefficient λ , with wave frequency for different Prandtl numbers. It is evident from the plot that the heat transfer coefficient tends to a maximum value at certain frequency and increases with increasing Prandtl number.

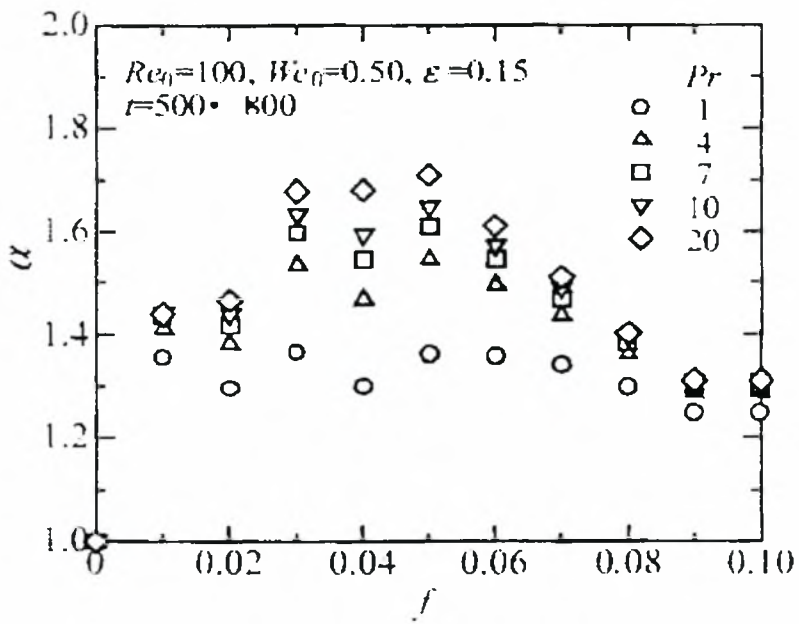


Figure 13. Variation of heat transfer enhancement with wave frequency

3. PROBLEM DEFINITION

In the present chapter we define the hydrodynamic problem of the development of nonlinear waves along the free surface of the film flow, as well as the thermal problem of heat transfer from the wall to the film. Among others we present the equations of the problems and the boundary conditions.

3.1 The flow problem

Two-dimensional, gravity-driven flow down a plane with inclination ϕ relative to the horizontal is considered. The mean volumetric flow rate per unit span is denoted by Q and the Re number is defined as $Re=Q/\nu$, where ν is the kinematic viscosity, $\nu=\mu/\rho$. Coordinate x is in the streamwise direction and coordinate y is normal to the plane. The location of the free surface and the magnitude of the instantaneous volumetric flow rate per unit span generally vary with x and t and are described by the functions $\eta(x,t)$ and $q(x,t)$ respectively. For reference we recall the classical Nusselt solution (developed in §2.1) for uniform flow with thickness, $h_N = (3\nu^2 Re/g \sin \phi)^{1/3}$, where g is the magnitude of gravity, and parabolic x -velocity profile given by

$$u(x, y, t) = \frac{g \sin \phi h_N^2}{\nu} \left(\frac{y}{h_N} - \frac{1}{2} \frac{y^2}{h_N^2} \right) \quad (3.1.1)$$

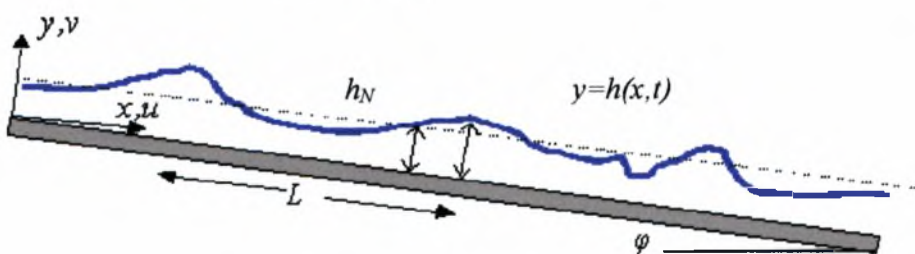


Figure 14. Sketch of the flow system considered

The mean Nusselt velocity in the x-direction is thus $U = g \sin \varphi h_N^2 / 3\nu$ and $Q = U h_N$.

A complete description of the flow is provided by the continuity and the Navier-Stokes equations, together with a set of boundary conditions. We use U as the characteristic velocity and h_N as the characteristic length and nondimensionalize time and pressure with the magnitudes h_N / U and ρU^2 respectively. The resulting equations in dimensionless form are:

$$\nabla \cdot \underline{u} = 0 \quad (3.1.2)$$

$$\frac{\partial \underline{u}}{\partial t} + \underline{u} \cdot \nabla \underline{u} = -\nabla p + \frac{1}{\text{Re}} \nabla^2 \underline{u} + \frac{1}{\text{Fr}} \underline{g} \quad (3.1.3)$$

Here $\underline{u} = (u, v)$ is the dimensionless velocity vector in the fluid, with u and v its components in the x- and y-direction, respectively, p is the dimensionless pressure and \underline{g} is the unit vector in the direction of gravity. Re is the Reynolds number as defined above and $\text{Fr} = U / \sqrt{gh_N}$ is the Froude number. Because of the way the equations are nondimensionalized, the Froude number is not independent but is related to the Reynolds number by the expression

$$\text{Fr}^2 = \frac{\text{Re}}{3} \sin \varphi$$

We further apply the no-slip and no-penetration boundary condition for the velocity along the flat wall,

$$u = v = 0 \quad (3.1.4)$$

and the kinematic condition and the balance of forces along the free surface:.

$$\frac{\partial h}{\partial t} + u \frac{\partial h}{\partial x} = v \quad (3.1.5)$$

$$\underline{n} \cdot \underline{T} = \text{We} 2H_c \underline{n} \quad (3.1.6)$$

The Weber number in eq. (3.1.6) is defined as $\text{We} = \sigma / \rho U^2 h_N$, with σ the surface tension of the fluid, $2H_c = h_{xx} / (1 + h_x^2)^{3/2}$ the mean free surface curvature, \underline{n} the unit vector normal to the free surface and

$$\underline{\underline{T}} = -p\underline{\underline{I}} + \frac{1}{\text{Re}} \left[\underline{\nabla}u + (\underline{\nabla}u)^T \right] \quad (3.1.7)$$

the dimensionless stress tensor of the fluid, with $\underline{\underline{I}}$ the identity matrix.

We apply the following boundary conditions at the inlet in order to introduce a small, periodic disturbance of frequency f and amplitude A in the film thickness:

$$h(0,t) = 1 + A \cos 2\pi f t \quad (3.1.8)$$

$$u(0,y,t) = \frac{3q(0,t)}{h(0,t)} \left[\frac{y}{h(0,t)} - \frac{1}{2} \frac{y^2}{h^2(0,t)} \right] \quad (3.1.9)$$

Equation (3.1.8) prescribes the oscillations of the free surface at the inlet of the computational domain and equation (3.1.9) imposes a parabolic velocity profile in the x -direction at the entrance. We will present, in a following paragraphs more details about the inflow boundary conditions, which are still the subject of study. The parabolic velocity profile is expected to be an excellent approximation for the entrance conditions, given the small magnitude of the disturbances. The corresponding inlet velocity, $v(0,y,t)$, in the y -direction is found by integration of the continuity equation using equation (3.1.9). (Lee & Mei, 1995)

At the outflow, we apply the free boundary condition in order to let the fluid leave the computational domain freely without any distortion of the flow in the interior (Malamataris & Papanastasiou, 1991) Finally, the steady state solution of the undisturbed free surface flow is used as the initial condition for the computation.

3.2 The thermal problem

Describing the thermal problem we consider the same field as in the flow problem. The heat transport takes place from the heated wall to the thin film which flows above it. A schematic view is in the Figure 15 below.

The flow is considered isothermal, with temperature T_a , up to a streamwise distance $x=x_0$ from the inlet, and then the wall is kept at a constant higher temperature, T_w where $T_w > T_a$. The free surface is thermally characterized by considering a uniform air temperature, T_a , and constant heat transfer coefficient, λ , from surface to air. The effect of temperature on the physical properties is neglected (passive scalar transport) and thus the flow and the heat transfer problems are solved consecutively.

A complete description of the thermal problem is provided by the energy equation and appropriate boundary conditions.

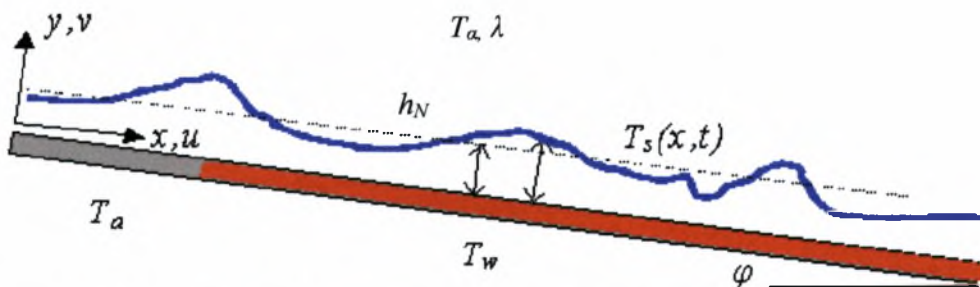


Figure 15. Inclined film flow with waves with heated wall.

As the flow is two-dimensional, incompressible, and there is no heat generation, the energy equation is:

$$\frac{\partial T}{\partial t} + (u \cdot \nabla)T - a \nabla^2 T = 0 \quad (3.2.1)$$

Here $(u \cdot \nabla)T$ accounts for heat convection with the flow and $a \nabla^2 T$ for molecular diffusion.

The boundary conditions are:

(1) The prescription of the imposed temperature on the wall:

$$y=0, x \leq x_0 \Rightarrow T = T_a$$

$$y=0, x \geq x_0 \Rightarrow T = T_w$$

(2) The energy balance at the interface. To be more specific this is the thermal energy balance in an infinitesimally thin control volume containing the interface. Given that the energy accumulation rate is

proportional to the volume, and thus goes to zero in the above control volume, we may write:

$$-\kappa \frac{\partial T}{\partial y} = \lambda(T - T_a) \Rightarrow \frac{\partial T}{\partial y} + wT = wT_a \quad (3.2.2)$$

where $w = \frac{\lambda}{\kappa}$ and κ is the thermal conductivity of the fluid $[\frac{W}{m \cdot K}]$

(3) The free outflow boundary condition at $x=L$, which is similar to the outflow condition of the flow problem.

As we want to nondimensionalize the above equations, we use $(T_w - T_a)$ as the characteristic temperature scale and the Nusselt film thickness, h_N , as the characteristic length. Symbolizing the dimensionless temperature by $\theta = (T - T_a)/(T_w - T_a)$ and keeping for brevity the same symbols for the dimensionless space and time variables, we obtain:

$$\frac{\partial \theta}{\partial t} + \underline{u} \cdot \underline{\nabla} \theta = \frac{1}{\text{Re} \cdot \text{Pr}} \nabla^2 \theta \quad (3.2.3)$$

where $\text{Pe} = \text{Re} \cdot \text{Pr}$ is the Peclet number.

The equation (3.2.2) in dimensionless form is:

$$\frac{\partial \theta}{\partial y} = \text{Bi} \theta \quad (3.2.4)$$

where Bi is the Biot number, $\text{Bi} = \lambda h_N / \kappa$.

The Peclet number is $\text{Pe} = \frac{U h_N}{\alpha}$, where U is the mean velocity of

the fluid $[\frac{m}{\text{sec}}]$, α the thermal diffusivity $[\frac{m^2}{\text{sec}}]$, h_N is the Nusselt film

thickness $[m]$. We can notice that Pe represents the ratio of heat transfer by convection to heat transfer by diffusion, and in this sense, is analogous to the Reynolds number for momentum transfer. Pr is the Prandtl number $\text{Pr} = \frac{\nu}{\alpha}$, with ν the kinematic viscosity of the fluid.

According to the nondimensionalization adopted for the temperature, $\theta_w = 1$ and $\theta_a = 0$. The trivial solution for a thermally

developed flat film with thermal conductivity, κ , is a linear temperature distribution with free-surface value

$$T_s = (T_w + BiT_a)/(1 + Bi) \quad (3.2.5)$$

(or, equivalently $\theta_s = 1/(1 + Bi)$). The linear temperature distribution is established because heat transfer occurs only in the vertical direction and only by diffusion. The steady heat transfer through this flat thermally developed film is: $q_0 = \kappa \frac{(T_w - T_s)}{h_N}$ and if we introduce equation

(3.2.5) we obtain:

$$q_0 = \frac{Bi}{(1 + Bi)} \kappa \frac{(T_w - T_a)}{h_N} \quad (3.2.6)$$

The value q_0 is used to nondimensionalize heat transfer through the wavy film. The problem is described in terms of the Pe and Bi dimensionless numbers. As initial condition we normally use a uniform temperature, T_a , throughout the film. This is equivalent to the physical situation where the heat source that sets the wall temperature is suddenly set on at $t=0$.

3.3 The inflow boundary conditions

The boundary condition at the entrance of the computational domain is the subject of continuing study which lies beyond the needs of the present work. As it has been mentioned, this boundary condition is time-dependent and introduces the disturbances that grow into free surface waves. Trying to simulate the conditions of experiments more closely, we use different forms of disturbances. This investigation leads to very interesting results regarding how the form of disturbance influences downstream evolution.

The sinusoidal perturbation $h(0,t) = -\alpha \sin 2\pi ft$ has been used many times in our computational efforts and it is known to perform excellently. The new form of perturbation presently introduced consists

of a series of influx surges, each corresponding to an inlet film thickness variation of Gaussian shape. Thus, the form of the perturbations is :

$$h(0, t) = \sum_{n=0}^{\infty} a e^{-\left(t-t_0 + \frac{n-1}{f}\right)^2 / 2\sigma^2} \quad (3.3.1)$$

where f is the frequency of the disturbance and σ is a parameter indicating the sharpness of the flow surge. Advantages of the present form of disturbance are (a) that it corresponds to positive mass surges and thus simulates more closely the experimental conditions, and (b) that it permits independent variation of the frequency and the steepness of the inlet waves.

In order to apply the above (or any other) inlet disturbance as a boundary condition at the liquid film inlet (boundary condition in $x=0$), it is necessary to know not only $h(0, t)$ but also $u(0, y, t)$ and $v(0, y, t)$ i.e. the local values of the components of the velocity in the $-x$ and $-y$ direction, respectively.

The function $h(0, t)$ has the form that we want to introduce, for example sinusoidal or Gaussian distribution. In the $x=0$ position the distribution of x -component of the velocity is considered parabolic according to the exact solution given by Nusselt theory. Thus:

$$u(0, y, t) = \frac{3Q(0, t)}{h(0, t)} \left(\frac{y}{h(0, t)} - \frac{1}{2} \frac{y^2}{h^2(0, t)} \right) \quad (3.3.2)$$

The velocity component in the y -direction, $v(0, y, t)$ is obtained by substituting (3.3.2) in the continuity equation, integrating in the vertical direction from $y=0$ up to an arbitrary location y and applying the no-slip boundary condition at the wall. The resulting expression is

$$v(0, y, t) = \left[\frac{\partial Q(0, t)}{\partial x} \frac{1}{2h^3(0, t)} - 3 \frac{\partial h(0, t)}{\partial x} \frac{Q(0, t)}{2h^4(0, t)} \right] y^3 - \left[3 \frac{\partial Q(0, t)}{\partial x} \frac{1}{2h^2(0, t)} - 3 \frac{\partial h(0, t)}{\partial x} \frac{Q(0, t)}{2h^3(0, t)} \right] y^2, \quad (3.3.3)$$

$$0 \leq y \leq h$$

In order to apply equations (3.3.2) and (3.3.3) we need to know the functions $h(x,t)$, $Q(x,t)$ and their spatial derivatives at $x=0$. The missing unknowns are found by considering that: (a) inlet disturbances initially travel with the phase velocity of small-amplitude waves, $c=3$, and (b) grow slowly enough at the inlet so that to a very good approximation their characteristics remain stationary for an observer traveling in the x direction with velocity c .

Considering the time variation of liquid film thickness in the above reference frame is equivalent to riding on a crest of the surface wave and following the flow. The result may be expressed as:

$$\left. \frac{dh}{dt} \right|_{\substack{\text{following} \\ \text{the wave} \\ \text{crest}}} = 0 \quad \text{or, according to the definition of the time derivative for a}$$

moving observer:

$$\frac{\partial h}{\partial t} + c \frac{\partial h}{\partial x} = 0 \quad (3.3.4)$$

The phase velocity, as we mentioned above is equal to 3, as found from linear stability analysis (§2.2). Equation (3.3.4) is used for the determination of the spatial derivative of the free surface, $\frac{\partial h}{\partial x}$, given that the temporal derivative, $\frac{\partial h}{\partial t}$, is readily found by differentiation of eq. (3.3.1).

Describing the flow rate in a similar way, we observe that its temporal and spatial derivatives are related by the expression:

$$\left. \frac{dQ}{dt} \right|_{\substack{\text{following} \\ \text{the wave} \\ \text{crest}}} = 0 \Rightarrow \frac{\partial Q}{\partial t} + c \frac{\partial Q}{\partial x} = 0 \quad (3.3.5)$$

By integrating the continuity equation in the vertical direction from the wall, $y=0$, to the free surface, $y=h(0,t)$, and using the Leibnitz formula for differentiating an integral we obtain the relation for $Q(0,t)$:

$$\int_0^{h(x,t)} \frac{\partial u(x,y)}{\partial x} dy = - \int_0^{h(x,t)} \frac{\partial v(x,t)}{\partial y} dy \quad (3.3.6)$$

For the first term we have: $\int_0^{h(x,t)} \frac{\partial u(x,y)}{\partial x} dy = \frac{d}{dx} \int_0^{h(x,t)} u(x,y) dy - u(h(x,t)) \frac{dh(x,t)}{dx}$

and taking in account the definition of the flow rate is:

$$\frac{\partial Q(x,t)}{\partial x} - u(h(x,t)) \frac{dh(x,t)}{dx} \quad (3.3.7)$$

From the second term of the equation (3.3.6) is:

$$\int_0^{h(x,t)} \frac{\partial v(x,t)}{\partial y} dy = \frac{d}{dy} \int_0^{h(x,t)} v(x,y) dy = v(h(x,t)) - v(0) \quad (3.3.8)$$

From the relations (3.3.7), (3.3.8) we obtain that:

$$\frac{\partial Q(x,t)}{\partial x} - u(h(x,t)) \frac{dh(x,t)}{dx} = -v(h(x,t)) \Rightarrow \frac{\partial Q(x,t)}{\partial x} = u(h(x,t)) \frac{dh(x,t)}{dx} - v(h(x,t))$$

However, according to the kinematic boundary condition, which holds at the position $y = h(x,t)$:

$$\frac{\partial h(x,t)}{\partial t} + u(x,y) \frac{\partial h(x,t)}{\partial x} = v(x,y)$$

Thus, we are led to the final result:

$$\frac{\partial Q(x,t)}{\partial x} = - \frac{\partial h(x,t)}{\partial t} \quad (3.3.9)$$

Equations (3.3.4) and (3.3.9) permit determination of all the remaining unknowns.

Equation (3.3.9) is the integral expression of mass conservation. We can justify this key expression with a different way of thinking. If we make the mass balance in the thin control volume of the figure below (Figure 16), we recognize that the net flow rate into the control volume (inflow – outflow), accumulates mass and thus results in the variation of the position of the free surface. In mathematical terms, the above mass balance is described by the expression:

$$[Q(x,t) - Q(x+dx,t)]dt = [h(x,t+dt) - h(x,t)]dx \Rightarrow \frac{\partial Q(x,t)}{\partial x} = - \frac{\partial h(x,t)}{\partial t}$$

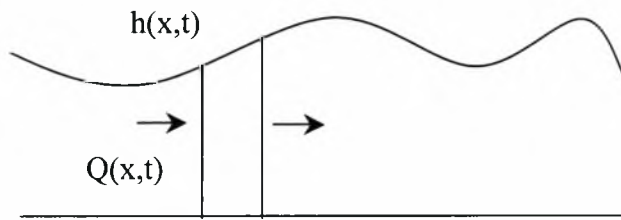


Figure 16. Differential mass balance in a thin control volume.

As we know the relation between $h(x,t)$ and $Q(x,t)$ we can introduce the temporal distributions of the inlet velocity components according to their expression (number of equations). The expected distributions of velocity components are evidently related to the kind of the initial disturbance $h(x,t)$ which we choose.

4. METHOD OF SOLUTION

This chapter describes the solution of the flow and the heat transfer problems by the Galerkin finite element method. We will explain, giving the appropriate details where necessary, the computational strategy and the actual implementation of the boundary conditions. Among others we present tips on which we are based for the development of key parts of the code.

4.1 Computational domain and solution grid

At the beginning we define the computational field as the geometrical domain in which the flow develops. The selection of computational field has to do with the problem definition and boundary conditions. We note at first that the physical domain extends from the inlet to the outlet in the x direction and from the wall to the free surface in the y direction. As the location of the free surface varies in time, it is convenient to nondimensionalize the y -distance in such a way that leaves the nodes of the elements unchanged. This is accomplished by nondimensionalizing the distance in the y direction by the local film thickness, $h(x,t)$, according to : $\hat{y} = \frac{y}{h}$. Thus, $\hat{y} = 0$ means that we are on the wall and $\hat{y} = 1$ corresponds to the free surface position.

Figure 16 shows a schematic view of the computational domain with the finite elements grid, according to the above definition. Thus, the location of each element in the computational domain is fixed in the transformed coordinates \hat{x}, \hat{y} , though the physical domain varies in time. As we will see later, the elements are nine-point isoparametric elements. The figure also shows the way of numbering of the elements. It should be noted that the grid density varies in the x direction, being denser at the beginning of the domain in order to rigorously simulate the start of the phenomenon.

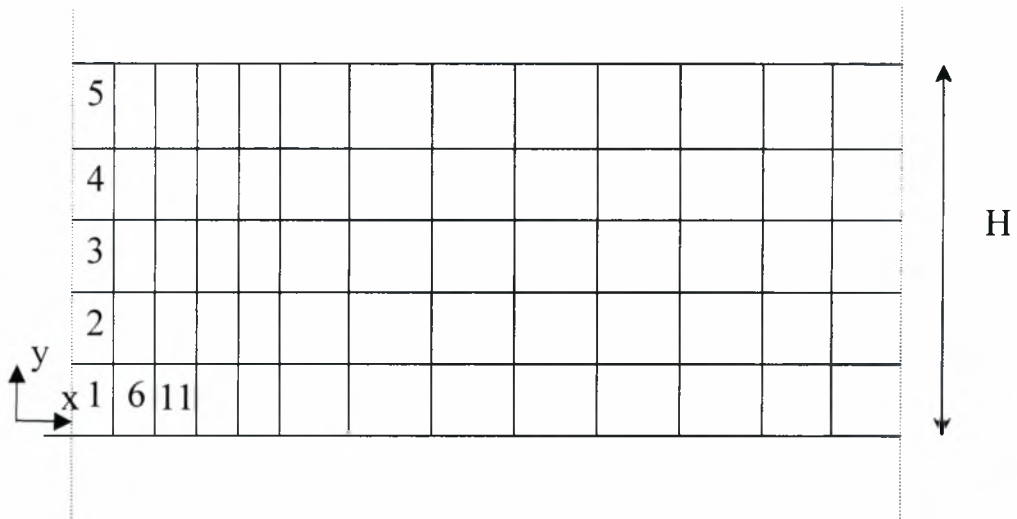


Figure 17. Computational domain and finite element' s grid .

The nodes are numbered in three different ways: local, coordinate, global. The way of numbering that we call local, is shown below (Figure 18), and it concerns the arrangement of nodes in each element. It is used extensively in the solution of the equations (computation of residual functions) because in the implementation of the finite element methodology the computation is performed in each element consecutively.

The global way of numbering is the absolute numbering of the nodes of mesh following the same concept as with the numbering of the elements, i.e. starting from the inlet and the wall and moving first towards the surface and then in the next x position. It is used in the storage of the unknown values (x , y , u , v velocities, pressure, temperature) in the respective arrays, with the global number providing the location in the array.

In the initial definition of the computational mesh, it is convenient to use the discretization in the x and y directions. Thus, we determine the location of each node by its x and y coordinates. We build up in this way a matrix of nodes, for example, the place (i,j) corresponds to the node that is found in the line i and in the column j . This constitutes the coordinate numbering.

Very often in the computational process, we need to switch from one to another system of numbering. Subroutine NODNOR (I,J) gives out the global number of a node, using as inlet the coordinate numeration. $NODNOR = (I-1)*NY+J$, where NY is the number of nodes in y-axes.

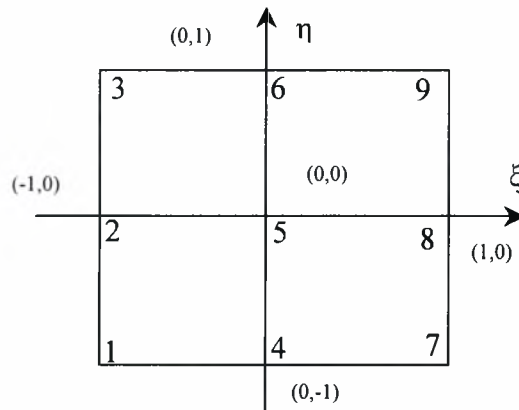


Figure 18. The pattern element and the local numeration of the nodes.

If we have the local number, J, of a node in the element NELL (the numbering of elements is shown in Fig. 15), then the function NOP(NELL,J) provides the global number of the node and permits the retrieval of node values, as in the following lines of code:

```
DO 102 J = 1, 9
  LN      = IABS(NOP(NELL,J))
  XE(J)   = X(LN)
  YE(J)   = Y(LN)
102 CONTINUE
```

4.2 Finite-element discretization of the unknowns

The problem is separated in two parts, flow and thermal, that are solved independently by the same code. To be more specific, the flow part is solved first, and then, using the latest results for the velocity field, we find the temperature field and the distribution of heat flux along the wall.

The primary unknowns of the problem, which are the velocities u and v , the pressure p and the temperature θ (dimensionalized), along with the unknown location of the free surface h , are expanded as follows

$$u = \sum_{i=1}^9 u_i \phi^i, \quad v = \sum_{i=1}^9 v_i \phi^i, \quad h = \sum_{i=1}^3 h_i \phi^i, \quad p = \sum_{i=1}^4 p_i \psi^i, \quad \theta = \sum_{i=1}^9 \theta_i \phi^i \quad (4.2.1)$$

where ϕ^i are biquadratic and ψ^i bilinear basis functions. This is a standard choice of basis functions in the application of the Galerkin finite element method in flow problems.

In the Galerkin finite elements method the equations for any given problem are solved in the pattern element, which has a local system of coordinates. Figure 16 shows the model element in the system of local coordinates (ξ, η) . The coordinates x, y change to ξ, η in the same way that the unknowns of the problem are expanded, based on Galerkin basis function:

$$x(\xi, \eta) = \sum_{i=1}^9 x_i \phi^i, \quad y(\xi, \eta) = \sum_{i=1}^9 y_i \phi^i \quad (4.1.2)$$

Equation (4.1.2) constitute the basic concept of isoparametric mapping, which is the process on which we are based in order to expand the unknowns of the problem in terms of Galerkin basis functions. Equation (4.1.2), as well as the exact form of the basis functions are provided by the following analysis.

We work on the pattern element (Figure 17) and we consider a type of interpolation with so many unknown coefficients as are the nodes of the element. Thus,

$$u(\xi, \eta) = a_1 + a_2 \xi + a_3 \eta + a_4 \xi \eta + a_5 \xi^2 + a_6 \eta^2 + a_7 \xi^2 \eta + a_8 \xi \eta^2 + a_9 \xi^2 \eta^2 \quad (4.2.2)$$

By applying the interpolating expression (4.2.2) to each of the nodes, we create an algebraic system of 9 equations which may be solved for the 9 unknown coefficients α_i , $i=1,9$. The system is: $u^e = \underline{C} \cdot \underline{a}$, where

$$\underline{\underline{C}} = \begin{bmatrix} 1 & -1 & -1 & 1 & 1 & 1 & -1 & -1 & 1 \\ 1 & -1 & 0 & 0 & 1 & 0 & 0 & 0 & 0 \\ 1 & -1 & 1 & -1 & 1 & 1 & 1 & -1 & 1 \\ 1 & 0 & -1 & 0 & 0 & 1 & 0 & 0 & 0 \\ 1 & 0 & 0 & 0 & 0 & 0 & 0 & 0 & 0 \\ 1 & 0 & 1 & 0 & 0 & 1 & 0 & 0 & 0 \\ 1 & 1 & -1 & -1 & 1 & 1 & -1 & 1 & 1 \\ 1 & 1 & 0 & 0 & 1 & 0 & 0 & 0 & 0 \\ 1 & 1 & 1 & 1 & 1 & 1 & 1 & 1 & 1 \end{bmatrix}$$

Thus, $\underline{\alpha} = \underline{\underline{C}}^{-1} \cdot \underline{u}^e$ (4.2.3)

Substituting equation (4.2.3) into (4.2.2), we obtain for a random point

$$\xi, \eta: u(\xi, \eta) = (1, \xi, \eta, \dots, \xi^2 \eta^2) \begin{pmatrix} \alpha_1 \\ \alpha_2 \\ \dots \\ \alpha_9 \end{pmatrix} = \underline{\beta} \cdot \underline{a} = (\underline{\beta} \cdot \underline{\underline{C}}^{-1}) \cdot \underline{u}^e \text{ and by defining :}$$

$$\underline{\varphi} = \underline{\beta} \cdot \underline{\underline{C}}^{-1} \Rightarrow \varphi^i = \beta_i \cdot C_{ij}^{-1} \quad \text{then} \quad u(\xi, \eta) = \underline{\varphi} \cdot \underline{u}^e = \sum_{i=1}^9 u_i \varphi^i(\xi, \eta). \quad \text{The basis}$$

functions are thus given by the expression :

$$\varphi^i = \beta_i \cdot C_{ij}^{-1} \tag{4.2.4}$$

The values of the unknowns u_i vary continuously from element to element because the values of the basis functions at the nodes satisfy the identity: $\varphi^i(\xi_i, \eta_i) = 1, \varphi^j(\xi_i, \eta_i) = 0, j \neq i$.

Expanding equation (4.2.4) we obtain the explicit dependence of the basis functions on ξ and η . A similar analysis may be followed for the 4-point element, and the final expressions for all the basis functions are the following:

$$\begin{aligned} \varphi(1) &= .25 * \xi * (\xi - 1.) * \eta * (\eta - 1.) \\ \varphi(2) &= .5 * \xi * (\xi - 1.) * (1. - \eta * \eta) \\ \varphi(3) &= .25 * \xi * (\xi - 1.) * \eta * (\eta + 1.) \\ \varphi(4) &= .5 * (1. - \xi * \xi) * \eta * (\eta - 1.) \\ \varphi(5) &= (1. - \xi * \xi) * (1. - \eta * \eta) \\ \varphi(6) &= .5 * (1. - \xi * \xi) * \eta * (\eta + 1.) \end{aligned}$$

$$\begin{aligned}\varphi(7) &= .25*\xi*(\xi+1.)*\eta*(\eta-1.) \\ \varphi(8) &= .5*\xi*(\xi+1.)*(1.-\eta*\eta) \\ \varphi(9) &= .25*\xi*(\xi+1.)*\eta*(\eta+1.)\end{aligned}$$

are the diquadratic basis function and :

$$\begin{aligned}\psi(1) &= .25*(1.-\xi)*(1.-\eta) \\ \psi(2) &= .25*(1.-\xi)*(1.+\eta) \\ \psi(3) &= .25*(1.+\xi)*(1.-\eta) \\ \psi(4) &= .25*(1.+\xi)*(1.+\eta)\end{aligned}$$

are the bilinear basis functions.

The derivatives with respect to ξ and η , are:

$$\begin{aligned}\varphi_{\xi}(1) &= \eta*(\eta-1.)*(.5*\xi-.25) \\ \varphi_{\xi}(2) &= (1.-\eta*\eta)*(\xi-.5) \\ \varphi_{\xi}(3) &= \eta*(\eta+1.)*(.5*\xi-.25) \\ \varphi_{\xi}(4) &= -\xi*\eta*(\eta-1.) \\ \varphi_{\xi}(5) &= -2.*\xi*(1.-\eta*\eta) \\ \varphi_{\xi}(6) &= -\xi*\eta*(\eta+1.) \\ \varphi_{\xi}(7) &= \eta*(\eta-1.)*(.5*\xi+.25) \\ \varphi_{\xi}(8) &= (1.-\eta*\eta)*(\xi+.5) \\ \varphi_{\xi}(9) &= \eta*(\eta+1.)*(.5*\xi+.25) \\ \varphi_{\eta}(1) &= \xi*(\xi-1.)*(.5*\eta-.25) \\ \varphi_{\eta}(2) &= (1.-\xi*\xi)*(\eta-.5) \\ \varphi_{\eta}(3) &= \xi*(\xi+1.)*(.5*\eta-.25) \\ \varphi_{\eta}(4) &= -\eta*\xi*(\xi-1.) \\ \varphi_{\eta}(5) &= -2.*\eta*(1.-\xi*\xi) \\ \varphi_{\eta}(6) &= -\eta*\xi*(\xi+1.) \\ \varphi_{\eta}(7) &= \xi*(\xi-1.)*(.5*\eta+.25) \\ \varphi_{\eta}(8) &= (1.-\xi*\xi)*(\eta+.5) \\ \varphi_{\eta}(9) &= \xi*(\xi+1.)*(.5*\eta+.25)\end{aligned}$$

If the unknown functions are interpolated in terms of the original spatial coordinates, we obtain expressions like :

$$u(x, y) = \gamma_1 + \gamma_2 x + \gamma_3 y + \gamma_4 xy + \dots \quad (4.2.5)$$

Switching between the (ξ, η) and the (x, y) coordinate systems imposes some consistency relations. More specifically, if we consider that

$u(\xi, \eta) = \sum u_i \varphi_i(\xi, \eta)$ and take in account that the nodes remain, in reality, the same:

$$u(x, y) = \sum u_i \varphi_i(\xi(x, y), \eta(x, y)) \quad (4.2.6)$$

So, if x_i, y_i are the nodes then: $u_i = \gamma_1 + \gamma_2 x_i + \gamma_3 y_i + \dots$ (4.2.7), and if we combine equations (4.2.5), (4.2.6), (4.2.7) then:

$u(x, y) = \sum (\gamma_1 + \gamma_2 x_i + \gamma_3 y_i + \dots) \varphi_i$, which means:

$$\gamma_1 + \gamma_2 x + \gamma_3 y + \dots = \gamma_1 \sum \varphi_i + \gamma_2 \sum x_i \varphi_i + \gamma_3 \sum y_i \varphi_i + \dots \text{ or :}$$

$$\sum \varphi_i = 1, x = \sum x_i \varphi_i, y = \sum y_i \varphi_i \quad (4.2.8)$$

These are the equations of isoparametric mapping as we introduced them above.

4.3 The integrally weighted governing equations

The governing equations of the flow, weighted integrally with the basis functions, result in the following continuity, R_C^i , momentum, R_M^i , and kinematic R_K^i residuals:

$$R_C^i = \int_V \nabla \cdot u \psi^i dV \quad (4.3.1)$$

$$R_M^i = \int_V \left(\frac{\partial u}{\partial t} + u \cdot \nabla u - \nabla \cdot \tau - \frac{1}{Fr} g \right) \varphi^i dV \quad (4.3.2)$$

$$R_K^i = \int_S \left(\frac{\partial h}{\partial t} + u \frac{\partial h}{\partial x} - \nu \right) \varphi^i dS \quad (4.3.3)$$

By applying the divergence theorem, in order to decrease the order of differentiation, equation (4.3.2)) reduces to:

$$R_M^i = \int_V \left[\left(\frac{\partial u}{\partial t} + \underline{u} \cdot \underline{\nabla} u - \frac{1}{Fr} \underline{g} \right) \varphi^i - \underline{T} \cdot \underline{\nabla} \varphi^i \right] dV - \int_S \underline{n} \cdot \underline{T} \varphi^i dS \quad (4.3.4)$$

where \underline{T} the dimensionless stress tensor of the fluid (see § 3.1).

Since essential boundary conditions for u and v are applied to all boundaries of the domain except at the outflow and along the free surface, equation (4.3.4) will be replaced by equations (3.1.4), (3.1.8) and (3.1.9). Along the free surface of the computational domain, the surface integrand of equation (4.3.4) will be replaced by equation (3.1.6). An interesting point in the implementation is the evaluation of equation (4.3.4) along the outflow. Instead of imposing some sort of boundary conditions (e.g. periodic), we extend the range of the Galerkin expansion up to and including the outflow. As a result, the outflow conditions come as part of the solution. This allows description of the developing flow without reflections caused by less efficient boundary conditions (Malamataris,1991).

The governing equation of the heat transfer problem, weighted integrally with the basis functions, results in the following residuals:

$$R_{\Theta}' = \int_V \left(\frac{\partial \theta}{\partial t} + u \cdot \underline{\nabla} \theta - \frac{1}{\text{Re Pr}} \nabla^2 \theta \right) \phi' dV = 0 \quad (4.3.5)$$

By applying the divergence theorem, in order to decrease the order of differentiation, equation (4.3.5) reduces

$$\text{to: } R'_{\Theta} = \int_V \left[\left(\frac{\partial \theta}{\partial t} - u \cdot \underline{\nabla} \theta \right) \phi' + \frac{1}{\text{Re Pr}} \underline{\nabla} \theta \cdot \underline{\nabla} \phi' \right] dV - \frac{1}{\text{Re Pr}} \int_S (\underline{\nabla} \theta \cdot \underline{n}) \phi' dS \quad (4.3.6)$$

The surface integral of equation (4.3.6) along the free surface is replaced by the boundary condition:

$$q = -\kappa \underline{\nabla} \theta \cdot \underline{n} = \lambda (\theta_w - \theta_\alpha) \quad (4.3.7)$$

4.4 Space and time integration algorithms

Implementation of the finite element methodology necessitates the computation of various spatial and temporal derivatives of the unknown functions and the incorporation of these computations in the evaluation of the residuals. The result is a nonlinear algebraic system of equations in terms of the node values of the unknown functions, which is numerically inverted to produce the solution.

Spatial derivatives are computed by applying the chain rule to move from the (x,y) to the (ξ,η) coordinate system. Thus:

$$\frac{\partial Z}{\partial x} = \frac{\partial Z}{\partial \xi} \frac{\partial \xi}{\partial x} + \frac{\partial Z}{\partial \eta} \frac{\partial \eta}{\partial x} \quad (4.4.1)$$

$$\frac{\partial Z}{\partial y} = \frac{\partial Z}{\partial \xi} \frac{\partial \xi}{\partial y} + \frac{\partial Z}{\partial \eta} \frac{\partial \eta}{\partial y} \quad (4.4.2)$$

The derivatives $\frac{\partial \xi}{\partial x}, \frac{\partial \xi}{\partial y}$, etc are evaluated from the transformation

expressions:

$$\frac{\partial x}{\partial x} = 1 \Rightarrow \frac{\partial x}{\partial \xi} \frac{\partial \xi}{\partial x} + \frac{\partial x}{\partial \eta} \frac{\partial \eta}{\partial x} = 1 \quad (4.4.3)$$

$$\frac{\partial x}{\partial y} = 0 \Rightarrow \frac{\partial x}{\partial \xi} \frac{\partial \xi}{\partial y} + \frac{\partial x}{\partial \eta} \frac{\partial \eta}{\partial y} = 0 \quad (4.4.4)$$

$$\frac{\partial y}{\partial x} = 0 \Rightarrow \frac{\partial y}{\partial \xi} \frac{\partial \xi}{\partial x} + \frac{\partial y}{\partial \eta} \frac{\partial \eta}{\partial x} = 0 \quad (4.4.5)$$

$$\frac{\partial y}{\partial y} = 1 \Rightarrow \frac{\partial y}{\partial \xi} \frac{\partial \xi}{\partial y} + \frac{\partial y}{\partial \eta} \frac{\partial \eta}{\partial y} = 1 \quad (4.4.6)$$

The equations (4.4.3), (4.4.6) consist an algebraic system of two equations, to which the unknowns are: $\frac{\partial \xi}{\partial x}, \frac{\partial \eta}{\partial x}$. The solution is:

$$\frac{\partial \xi}{\partial x} = \frac{\partial y / \partial \eta}{J}, \frac{\partial \eta}{\partial x} = \frac{-\partial y / \partial \xi}{J} \quad (4.4.7)$$

where $J = \frac{\partial x}{\partial \xi} \frac{\partial y}{\partial \eta} - \frac{\partial x}{\partial \eta} \frac{\partial y}{\partial \xi}$ is the Jacodian determinant.

According to the former method, equations (4.4.4) and (4.4.5) form a similar system and have as solution the following expressions for $\frac{\partial \xi}{\partial y}, \frac{\partial \eta}{\partial y}$.

$$\frac{\partial \xi}{\partial y} = \frac{-\partial x / \partial \eta}{J}, \frac{\partial \eta}{\partial y} = \frac{\partial x / \partial \xi}{J} \quad (4.4.8)$$

The derivatives $\frac{\partial x}{\partial \xi}, \frac{\partial y}{\partial \xi}$ etc are computed directly by the expressions (4.2.8) for isoparametric mapping. Thus:

$$\frac{\partial x}{\partial \xi} = \sum x_i \frac{\partial \varphi_i}{\partial \xi}, \frac{\partial y}{\partial \xi} = \sum y_i \frac{\partial \varphi_i}{\partial \xi} \quad (4.4.9)$$

$$\frac{\partial x}{\partial \eta} = \sum x_i \frac{\partial \varphi_i}{\partial \eta}, \frac{\partial y}{\partial \eta} = \sum y_i \frac{\partial \varphi_i}{\partial \eta} \quad (4.4.10)$$

Evaluation of temporal derivatives needs to take into account the variation of the physical grid with time. In particular, the partial derivative in time at a given location cannot be simply computed as $\frac{Z(n+1) - Z(n)}{dt}$, because during the time step dt the node has moved in physical space. Using the expression for the time derivative in a moving coordinate system, we obtain :

$$\frac{\partial Z}{\partial t} = \frac{dZ}{dt} - w \cdot \nabla Z = \frac{dZ}{dt} - \frac{\partial Z}{\partial x} \frac{\partial x}{\partial t} - \frac{\partial Z}{\partial y} \frac{\partial y}{\partial t} \quad (4.4.11)$$

The velocity of the point in question is found from the time variation of the physical location of the nodes. More specifically, we note that the regriding during each time step displaces the nodes only in the y direction. Thus, $u = \frac{y(n+1) - y(n)}{dt}$ and the partial time derivative is found equal to :

$$\frac{\partial u}{\partial t} = \frac{du}{dt} - \frac{\partial u}{\partial y} \frac{\partial y}{\partial t} \quad (4.4.12)$$

The residuals are evaluated numerically using nine-point Gaussian integration. A system of non-linear algebraic equations results, which is solved with the Newton-Raphson iterative method according to the

scheme: $\underline{q}^{(n+1)} = \underline{q}^{(n)} - \underline{J}^{-1} \underline{R}(\underline{q}^{(n)})$ where $q^T = [u_1, v_1, p_1, h_1, \dots, u_N, v_N, p_N, h_N]$ is the vector of the unknowns and $\underline{J} = \partial \underline{R} / \partial \underline{q}$ is the Jacobian matrix of the residuals \underline{R} with respect to the nodal unknowns \underline{q} . The banded matrix of the resulting linear equations is solved with a frontal solver (at each iteration. The Newton iteration of all efforts converged quadratically in 3-6 iterations, independent of the mesh resolution.

Time marching has been performed with the Crank-Nicolson scheme. More specifically, for an equation of the form $\frac{\partial z}{\partial t} = F(z)$, we use

the implicit scheme:

$$\frac{z(n+1) - z(n)}{dt} = \frac{1}{2} [F(z(n)) + F(z(n+1))] \quad (4.4.13)$$

which transforms the above differential equation into an implicit equation of differences.

5. RESULTS AND DISCUSSION

The results of our study are presented in this chapter. We apply the previously developed computational methodology to study the effect of waves on heat transfer from the wall. We first consider a flat film as a preliminary validation case. Then, we concentrate on the effect of a fully developed solitary wave train.

5.1 Heat transfer in flat film

In order to testify the validity of the code, we first carry out simulations for the case where the film is flat. For this simple case we can estimate the flow of the heat, just trusting our natural intuition. The results corresponds to four Pe numbers, namely 10,50,200,1000. For each Pe number, a diagram is presented, which describes the temperature profile across the film at different downstream locations.

As a general remark figures 19a-19d are quite similar. The slope of the lines on the wall gives the heat flux at the specific position x . Sharper slope indicates higher heat flux. In each case the last straight line represents the thermally full-developed field. This corresponds to steady state conditions, where the quantity of heat which enters in the fluid, leaves the film through the surface. The other lines indicate how the temperature profile varies through the fluid as the thermal field is developing.

It is noted that, the heat flux has been nondimensionalized with respect to the heat flux, q_0 , corresponding to the thermally fully developed flat film. The value q_0 has previously been derived analytically (equation 3.2.6).

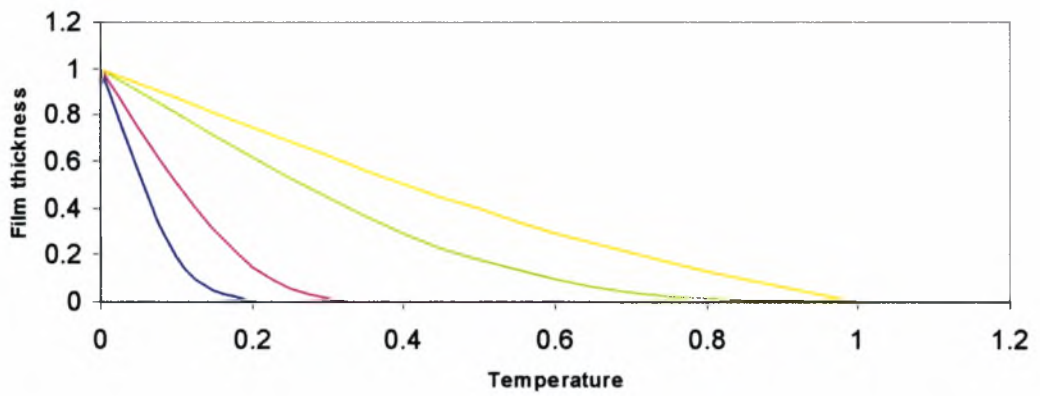


Figure 19a. The distribution of the temperature for $Pe=1000$, at four different x -positions.

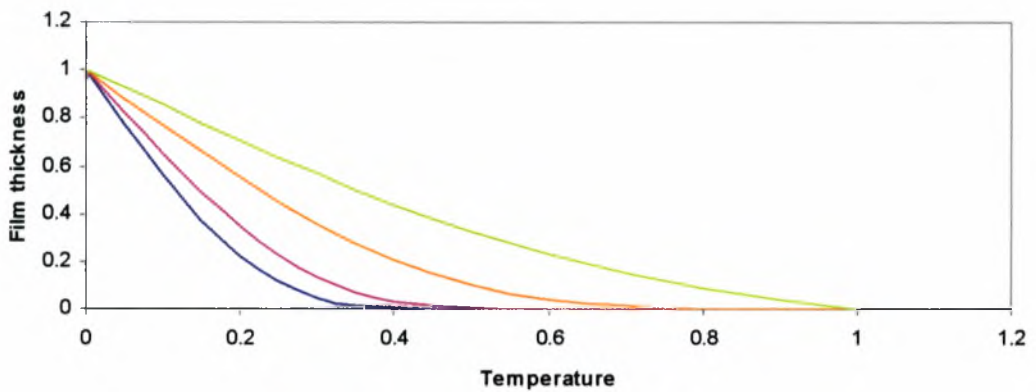


Figure 19b. The distribution of the temperature for $Pe=200$, at four different x -positions.

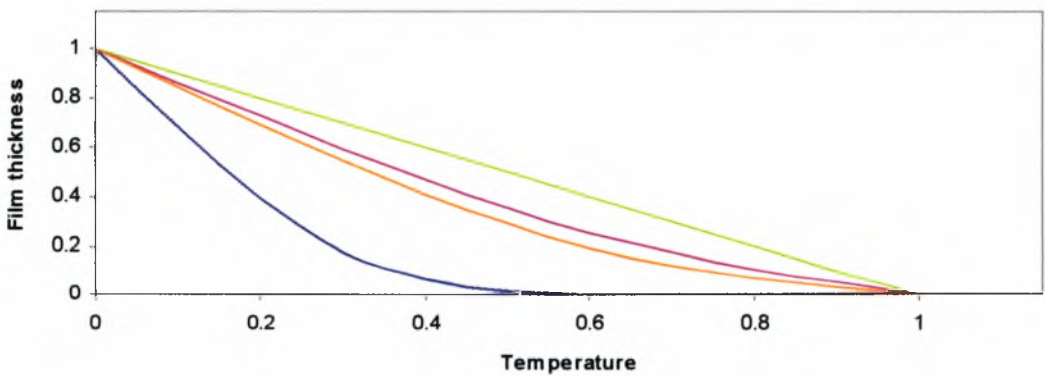


Figure 19c. The distribution of the temperature for $Pe=50$, at four different x -position.

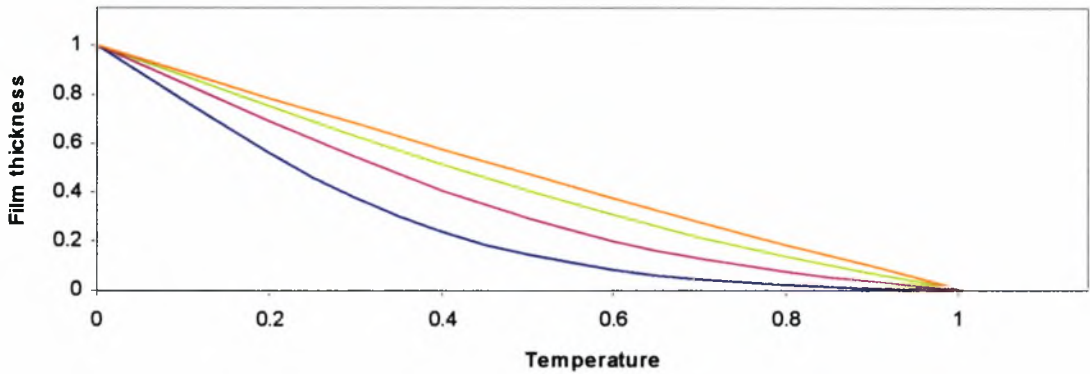


Figure 19d. The distribution of the temperature for $Pe=10$, at four different x-positions.

The next figure (Figure 20) shows the spatial variation of the wall heat flux for the different Pe numbers .

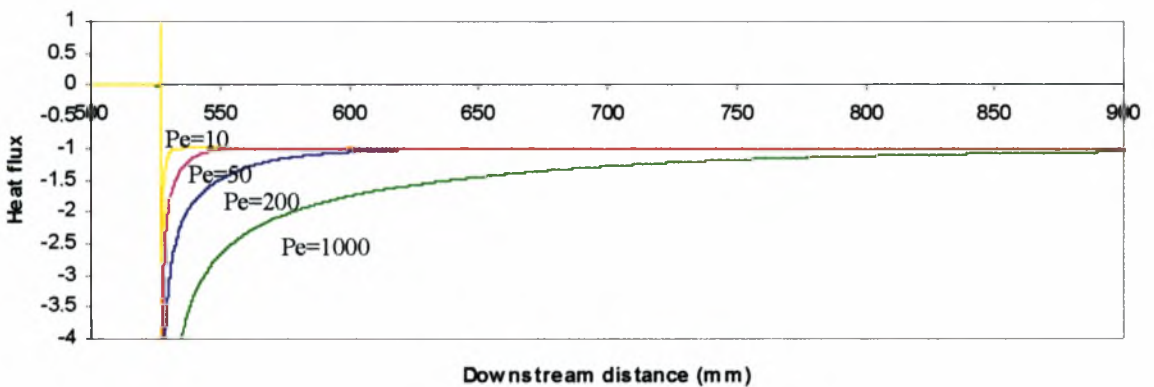


Figure 20. The heat flux from the wall for 4 Peclet number: 10, 50, 200 and 1000

From Figures 19a-19d, it is confirmed that the higher the Pe number the longer distance needed for the development of the thermal profile. Second, the slope of the curves becomes sharper as the Pe decreases. This indicates that the heat transfer from the wall to the liquid very close to the wall is more efficient for smaller Pe .

5.2 Wavy film: The flow field

In this section we present computer simulations of transient wave growth according to the finite-element methodology outlined in chapter 4. We report computer results under conditions (54% by weight glycerol in water, $\varphi=6.4^\circ$, $Re=19.33$, sinusoidal inlet disturbances with frequency 1.5) that simulate the experiments of Liu & Gollub (1994).

The following figure (Figure 21) shows the free surface profile at four different time instants. Five consecutive solitary crests are contained in each instant. We can notice, that the nonlinear evolution of the disturbance occurs through a gradual bending-forward of the crest, which triggers the development of front-running ripples. The number of ripples increases with the height of the crest.

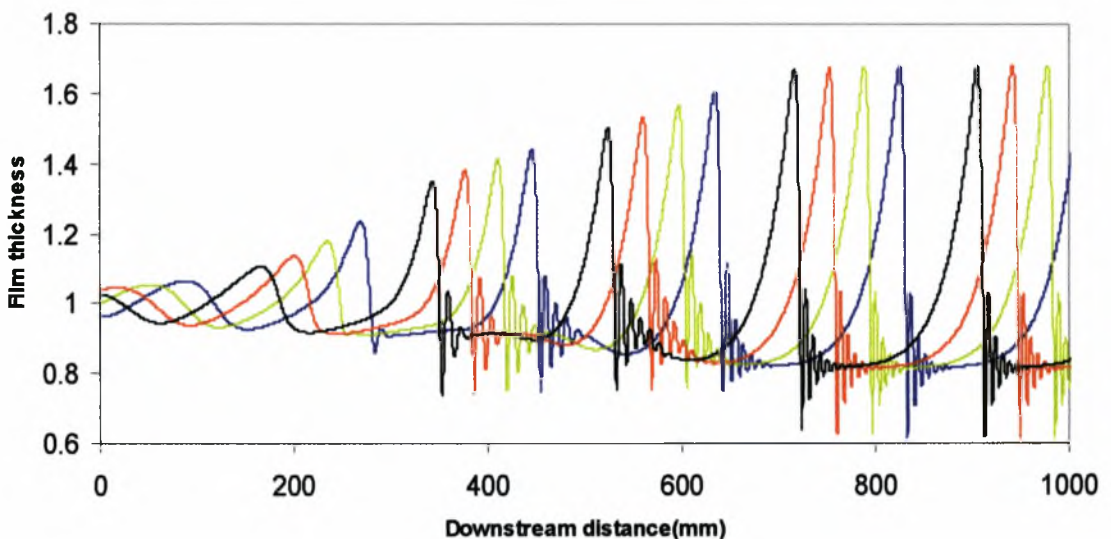


Figure 21. The formation of a series of a stationary solitary waves.

The first solitary crest is in the initial stages of development, while the last two appear to have reached the stationary stage, and thus travel at constant phase velocity, without further change in shape. The flow field imposed by the stationary waves is the one on which we are based in order to solve the thermal problem.

5.3 Heat transfer to the wavy film: transient phenomena

We note at first that, though the present flow problem is fully developed, the thermal is not. If we consider the wall heat source turned on at time zero, we first have a strong temporal transient because of the very high temperature gradients close to the wall. Representative results are shown in Figure 22, where the dimensionless heat flux from the wall is plotted as a function of spatial position for four consecutive time instants. We observe the expected drastic decrease of the mean spatial heat flux with time, which is characteristic of the initial transient. It is also interesting to observe that the passage of a wave has a very strong effect at the initial time instants.

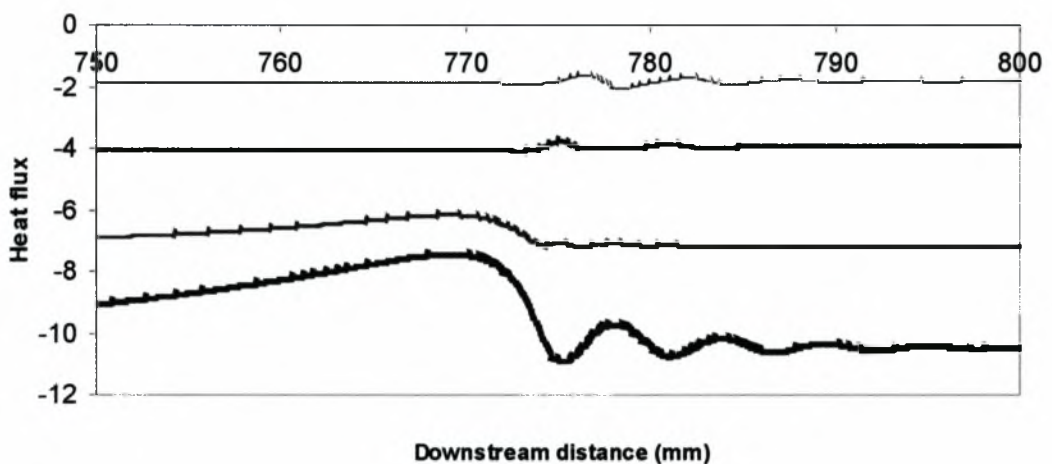


Figure 22. The heat flux from the wall for $Pe=10$ in four consecutive time instants.

The time needed for the initial transient to fade out is expected to depend on Pe number. Thus, to compare the results for different Pe , it is necessary to take into account the pertinent time-scale of transient effects.

If heat transfer was taken place purely by conduction, the characteristic time would be determined by the thermal diffusivity and would be equal to $t_0=h_N^2/\alpha$. Thus, we use t_0 in order to compare in

Figure 23 results for two very different Pe numbers, 10 and 1000. More specifically, we plot the respective heat flux distributions at respective instants which correspond to the same dimensionless time when nondimensionalized with t_0 .

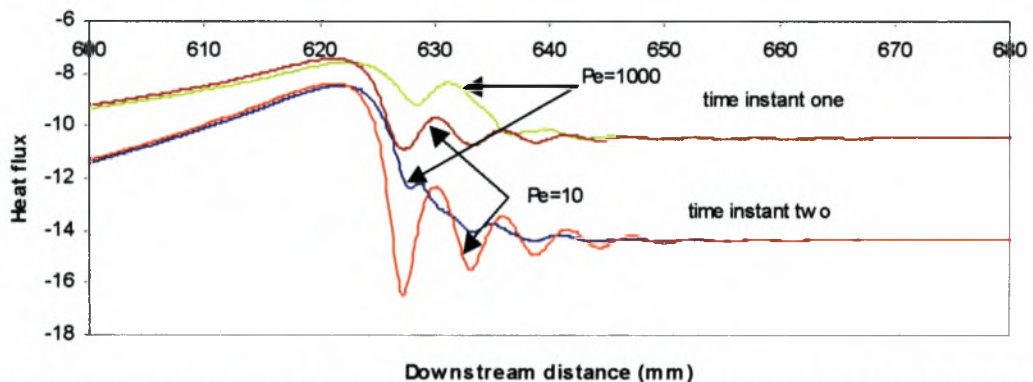


Figure 23. The heat flux from the wall giving from 2 Pe number:10,1000 in two different time instants.

Figure 23 shows that there is perfect coincidence of the results for the two different Pe numbers over the flat portion of the film. This was to be expected given the local lack of convection, and simply confirms the correct selection of characteristic time t_0 . As convection is provided only by the velocity component normal to the wall, we expect it to become significant only under the high-slope regions of the solitary wave profile, where the v -component of velocity is non-negligible. Indeed, the differences in each pair of curves of Figure 23 are a manifestation of the effect of convection.

5.4 Wavy film: The thermally quasi-developed flow

Next we consider the thermal behavior after sufficient time for the transient behavior to fade. The flow corresponds to the conditions of the experiment of Liu & Gollub, ie. $Re=19.33$, $We=5.43$, $\varphi=6.4^\circ$ and $f=1.5$ Hz. Note that the flow is created so that it has become stationary before point x_0 , ie the solitary waves have attained a permanent shape and move with constant phase speed. In general, the downstream location

where the system becomes hydrodynamically fully developed is easily modified by controlling the amplitude of inlet disturbances. The flow conditions tested (small Re and inclination angle) do not produce waves with internal recirculation [Malamataris et al, 2002]. The enhancement of wall heat transfer under such conditions has previously been attributed [Jayanti & Hewitt, 1995] mainly to the thinning of the liquid film, which is caused by the accumulation of mass in the solitary humps. The present rigorous simulation provides a means of investigating in detail the relative effects of conduction and convection under the mild flow conditions imposed. It is recalled that vertical films at higher Re show significant enhancement, which was shown [Miyara,1999] to be related to the recirculating region developing under the crests.

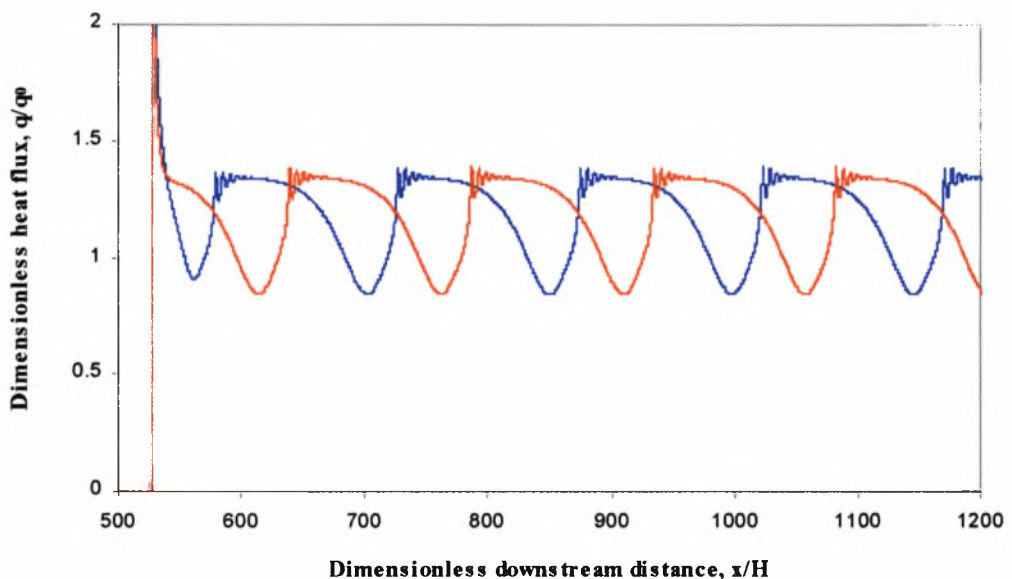


Figure 24. The spatial distribution of the wall heat flux for $Pe=50$, at two different time instants separated by 20 dimensionless time units.

Once the initial transient has faded away, the spatio-temporal evolution is only dictated by the passage of the solitary waves. Figure 24 shows such an example, which refers to the distribution of the wall heat flux for $Pe=50$, at two different instants separated by 20 dimensionless time units. A striking observation is that—beyond a rather

short development region— a spatially periodic distribution of the heat flux appears, which is in correspondence to the instantaneous location of the solitary waves and moves with their constant phase velocity. This flux distribution indicates that the thermal problem reaches a quasi-steady state, an observation that should be expected because of the large thickness of the wall thermal boundary layer ($Pr=0.5-10$) compared to the thickness of the liquid film.

In order to investigate the effect of Peclet number, we consider a range of values ($Pe=5-200$). Figure 25 shows one period of the spatial distribution of the wall heat flux (in the quasi steady-state) for three representative cases.

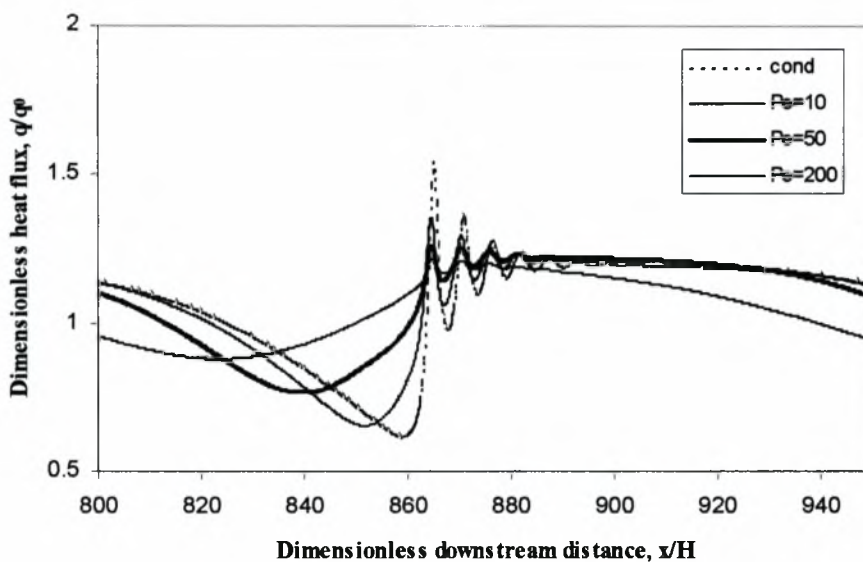


Figure 25. The spatial distribution of the wall heat flux for different Pe numbers.

Also included is the hypothetical distribution, where the heat flux at each location corresponds to a thermally developed flat film with the local thickness. The latter is considered a satisfactory approximation of the effect of pure conduction in the long-wave limit. Figure 25 demonstrates the effect on wall heat flux of two different time (or length) scales associated with the passage of solitary waves. The shortest

scale corresponds to the oscillations of the front-running ripples. It is seen to affect heat transfer significantly less than in the conduction limit, and its net effect appears to be low. The longer scale corresponds to the wavelength of the solitary train, and it affects all the Peclet number values considered. In particular, for Peclet number < 50 the thermal behavior of the thin substrate between crests is roughly equivalent to pure conduction. These predictions can be explained by considering that the passage of each wave temporarily forces fluid parcels to approach the wall, while at the same time decelerates and elongates them in the streamwise direction. The extent of additional transient conduction taking place under these conditions is evidently dictated by the relation of the characteristic thermal diffusion time to the aforementioned flow oscillation scales.

In addition to the above, Figure 25 demonstrates a nonlinear phenomenon associated with the crest of the waves. In the conduction limit, the crest offers the highest resistance to heat transfer, and thus mitigates the positive effect of the thin substrate. However, we presently observe that, with increasing Peclet number, the minimum of the wall heat flux is raised significantly and is also shifted behind the wave crest. This behavior is associated with the thermal inertia of the fluid masses transported by the solitary humps and is also manifested in the temperature field below the wave, which is depicted in Figure 26a-d. More specifically, the temperature iso-contours –which at small Peclet number are roughly self-similar to the shape of the free surface– gradually become convection-dominated, with a sharp peak at the front of the solitary hump and a weak maximum under the tail.

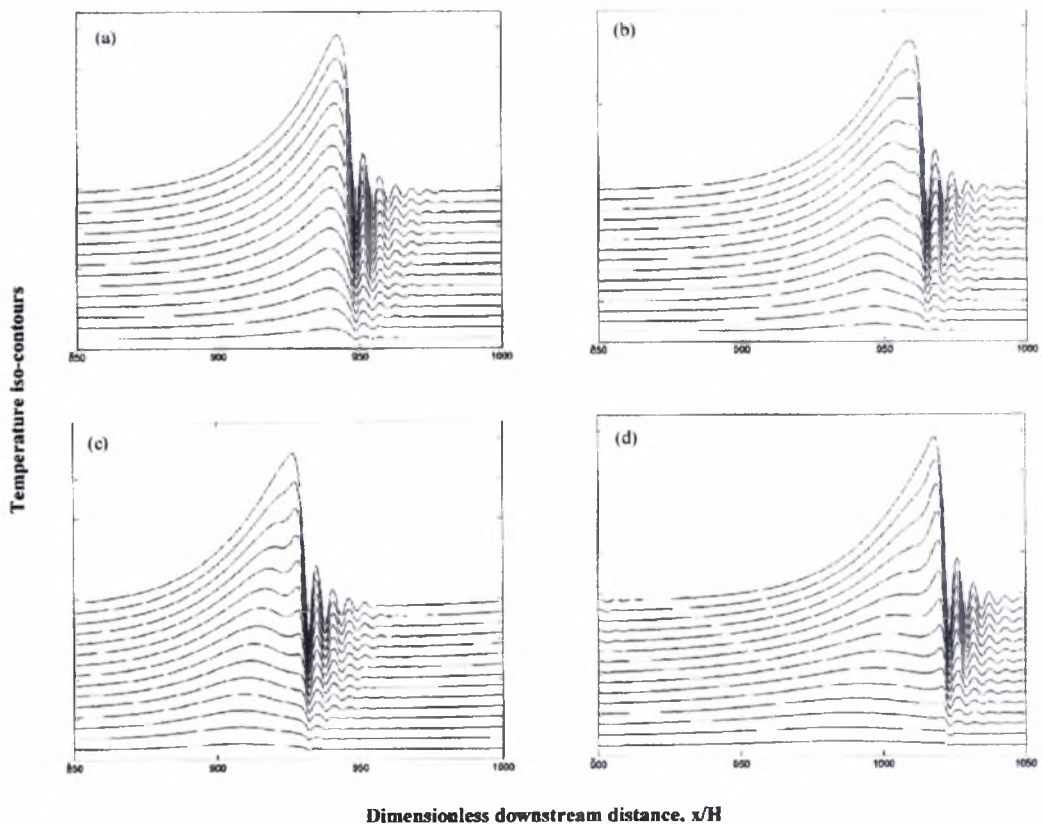


Figure 26. Quasi-steady temperature distribution below the wave for different Pe numbers. (a) Pe=5, (b) Pe=25, (c) Pe=50 and (d) Pe=200.

The mean heat flux through the wall (resulting from a combination of all the above contributions) is shown as a function of Peclet number in Figure 27. The value for Peclet number 0.01 corresponds to the conduction limit of Figure 25. It is interesting to note that a significant enhancement beyond the conduction limit is predicted for a wide range of Peclet numbers. Thus, the present computation supports the conclusion that convection contributes significantly to the wall heat transfer even when the solitary waves do not have a strong recirculation.

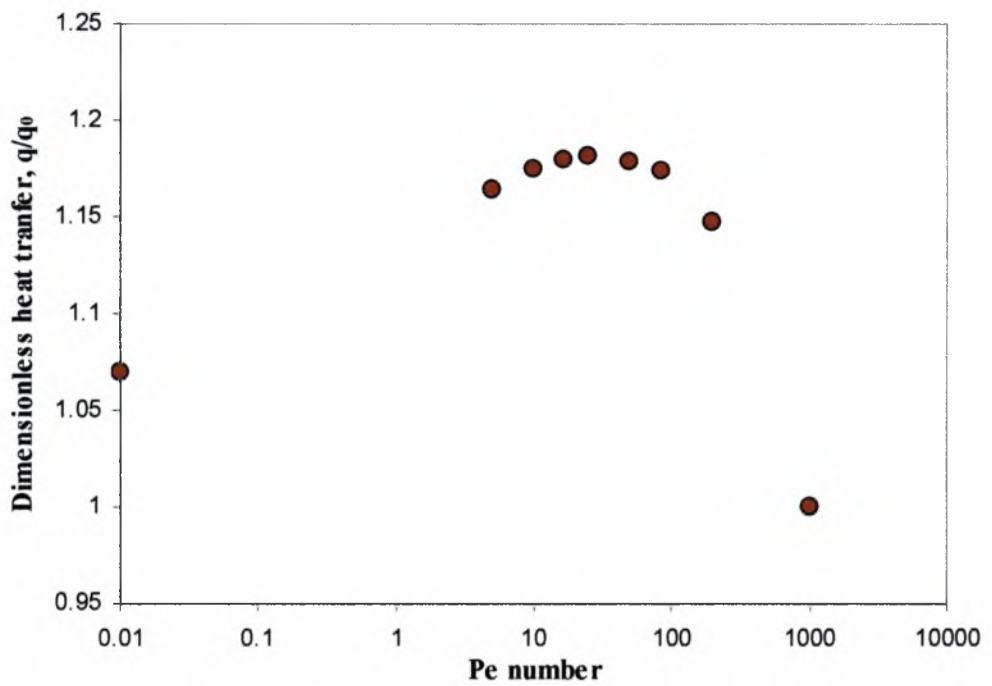


Figure 27. The mean wall heat flux along one wavelength as a function of Pe number.

6. CONCLUDING REMARKS

The main conclusions from the present work are the following:

- The thermal energy balance has been incorporated in a Galerkin finite-element scheme, and the code has been used to study heat transfer from an isothermal wall to an inclined liquid film.
- Validation results for a flat film agree with the analytic solution in the steady-state limit. They also demonstrate the effect of Peclet number on the heat flux from the wall and on the extent of the thermally developing length.
- Detailed results are derived on the effect of a regular solitary wavetrain on heat transfer from the wall. More specifically, it is found that:
 - A stationary, spatially periodic flux distribution develops, which follows the waves.
 - The smaller the Peclet number the stronger the oscillation of the heat flux around the mean value.
 - Convection, imposed by the vertical wavy motions has a non-negligible impact on heat transfer, particularly at the crest and the tail of the solitary waves.
- For a wide range of Peclet numbers, the effect of convection, in combination with the thinning of the substrate between successive waves, results in heat transfer enhancement significantly above the conduction limit.

REFERENCES

1. Alekseenko, S.V., Nakoryakov, V. Y., and Pokusaev, B. G., "Wave formation on a vertical falling liquid film," *AIChE J.* **31**, 1446-1460 (1985).
2. Alekseenko, S.V., Nakoryakov, V. Y., and Pokusaev, B. G., Wave flow of Liquid film, *Begell House*, (1994).
3. Bays, G.S., Adams, W.H., Heat transfer coefficients in falling film heaters streamline flow, *Industr. Engin. Chem.* **29**,11, 1240-1246, (1937)
4. Batchelor, G.K, An introduction to fluid dynamics, *Cambridge Mathematical Library, Cambridge University Press* (2000).
5. Billingham, J., & King, A.C., Wave motion, *Cambridge texts in applied Mathematics, Cambridge University Press* (2000).
6. Bird, R., Stewaed, W., Lightfoot, E., Transport phenomena, *John Wiley & Sons, Inc*, (1960).
7. Chang, H.-C., "Wave evolution on a falling film", *Annu. Rev. Fluid Mech.* **26**, 103-136 (1994).
8. Chang, H.-C., Demekhin, E.A., Complex Wave dynamics on Thin Films, *Studies in Interface science, Elsevier*, (2002).
9. Chang, H.-C., Demekhin, E.A and Saprikin, S.S, " Noise-drive wave transitions on a vertical falling film", *J. Fluid Mech*,**294**, 123 (1995).

10. Cheng, M., Chang, H.-C., "Stability of axisymmetric waves on liquid films flowing down a vertical column to azimuthal and streamwise disturbances", *Chem Engrg. Comm.*, 327-40 (1992a).
11. Chernobylsky, I.I., Vorotsov, E.G., "Hydrodynamics and heat transfer to flooding liquid films at its gravitational flow along the vertical surface of heat transfer", in *Heat and Mass Transfer (in Russian)*, M. Enegiya, **1**, 259-266 (1968).
12. Chu, K.J., Dukler, A.E., " Statistical characteristics of thin wave films, *Aiche J.*,**20**,4, 695-706 (1974).
13. Gimbutis, G., "Heat Transfer in gravitational flow of liquid films (in Russian), *Vilnyus, Mokslas*,232- (1988).
14. Graetz, L., Uder die Warmeleitbahigkeit von Flussigkeiten, *Ammalen de Physik*,**25**, 337-357 (1885).
15. Jayanti S., & Hewitt, G.F., "Hydrodynamics and heat transfer of wavy thin film flow", *Int. J. Heat Mass transfer* **40**, 179-190 (1997).
16. Kapitza, P.L., Kapitza, S.P, "Wave flow of thin layers of viscous fluid (in Russian), *Zhurm.Eksper. Teor. Fiz.*, **19**, 2, 105-120 (1949).
17. Lee J.J., & Mei, S.C., "Stationary waves on an inclined sheet of viscous fluid at high Reynolds and moderate Weber numbers", *Journal of Fluid Mechanics* **307**, 191-229 (1996).
18. Limberg, H., " Warmeubergang an turbulente und laminare Rieselfilm", *Int. J. Heat Mass Transfer*,**16**,9,1691-1702 (1973).

19. Lin, S.P., " Film waves. Waves fluid interface", Proc. Symp., Madison, Wisc., 18-10 Oct, New York, 261-289 (1983).
20. Liu J., Gollub, J.P., "Solitary wave dynamics of film flows", *Phys. Fluids*, **6**, 1702-1712 (1994).
21. Malamataris, N., Vlachogiannis, M., Bontozoglou, V., "Solitary waves on inclined films: Flow structure and binary interactions", *American Institute of Physics* **14**, number 3, (2002).
22. Malamataris, N.A., & Papanastasiou, T. C., "Unsteady free surface flows on truncated domains," *Ind. Engng. Chem. Res.* **30**, 2210 (1991).
23. Miyara, A., " Numerical analysis on flow dynamics and heat transfer of falling liquid film with interfacial waves", *Int. J. Heat and Mass transfer* **35**, 298-306 (1999).
24. Miyara, A., " Numerical simulation of wavy liquid film flowing down on a vertical wall and an inclined wall", *Int. J. Thermal Sciences* **39**, 1015-1027 (2000).
25. Miyara, A., " Flow dynamics and heat transfer of wavy condensate film", *Journal of heat transfer* **123**, 492-500 (2001).
26. Miyara, A., Nasoko, T., Nagata, T., " Enhancement of heat and mass transfer by waves on falling liquid film", *Proceedings, 12th International Heat Transfer Conference* , **2**, 591-596 (2002).

27. Nusselt, W., "Die Oberflächenkondensation des Wasserdampfes" Zeitschrift VDI, **60**, 541-546 (1916).
28. Pozrikidis, C., Introduction to theoretical and computational fluid dynamics, *Oxford University Press* (1997).
29. Pozrikidis, C., Numerical computation in science and engineering, *Oxford University Press*, (1998).
30. Prokopiou, T., Cheng, M., Chang, H.-C., "Long waves on inclined films at high Reynolds number", *J. Fluid Mechanics*, **222**, 665-691 (1991).
31. Ramaswamy, B., Chippada, S., & Joo, S.W., "A full-scale numerical study of interfacial in thin-film flows", *Journal of Fluid Mechanics* **325**, 163-194 (1996).
32. Serifi, K., Malamataris, N., Bontozoglou, V., "Transient flow and heat transfer phenomena in inclined wavy films", *Int.J of Thermal Sciences*, to be published (2004).
33. Sexauer, T., "Der Wärmeübergang am senkrechten berieselten", *Rohr. Forsch. Ing. Wes.*, **10**, 6, 286-296 (1939).
34. Sobin, V.M., "Heat transfer in a falling liquid film at thermal initial region (in Russian), *Inzh-Fiz. Zhurn*, 39, 4, 592-596 (1980).
35. Strahltrager, E., Miyara, A., Uehara, H., "Flow dynamics and heat transfer of a condensate film on a vertical wall-II. Flow dynamics and heat transfer", *Int. J. Heat and Mass transfer* **38**, 2715-2722 (1995).

36. Tananaiko, Yu.M., Vorotsov, E.G., "Methods of calculation and investigation into film processes (in Russian), Kiev, Thekhnika, 312- (1975).
37. Vorotsov, E.G., "The thermal diffusivity of falling films", *Theoretical foundations of Chemical Engineering* **33**, 99-108 (1999).
38. Vorotsov, E.G., Tananaiko, Yu.M., "Heat transfer in a liquid films", (in Russian), Kiev, Tekhnika, 194- (1972).
39. Vlachogiannis, M., Bontozoglou, B., " Observations of solitary wave dynamics of film flows", *J. Fluid Mech.*, **435**, 191 (2001).
40. Wilke, W., "The measurement of velocities in thin films of liquid, *Chem Ebg Sci*, **17**, 177-187 (1962).
41. Yih, C.S., "Stability of liquid flow down an inclined plane", *Phys. Fluids*, **6**, 321-334 (1963).
42. Zhukauskas, A., Zhyugzhda, I., "Heat transfer in laminar liquid flow", Vilnyus, Mintis, 261- (1969).

Appendix

List of the main subroutine of the thermal problem

```
SUBROUTINE TH_FIND
C
  PARAMETER (NXNP=313000,ND=145000,NL=31000,NCRIT=39,NG=19999)
C
  IMPLICIT REAL*8 (A-H,O-Z)
C
  COMMON /DERMAP/ DXDH(9,3),DYDH(9,3)
  COMMON /JACOB/ XC,XEDA,YC,YEDA,Y1,AY1,CX,CY,EX,EY
  COMMON /INDATB/ ERRMAX,IFPRNT,MAXITE
  COMMON /MESH/ NEX1,NEX4,NEX,NEY,NX,NY,NX1,NX14,NX2,NXFR,NXP
  COMMON /INOUT/ NCR,NLP,NCO,NSA,NPP,NLI,NHI,NTR,NSH
  COMMON /GSPNT/ GPX(9),GPY(9),GWEI(9),GPT(3),GWE(3)
  COMMON /INOT/ TSTEP,TIME,TMAX,TIME1,ICONT,NSTEP,IPRD,IPERT,ISTEP
  COMMON /FRON1/ NP,NH,NHADD,NE,NOP(NL,12),ND1,NELL,NTRA
  COMMON /TH_FRON2/ TH_NOPP(ND),TH_MDF(ND),TH_NBN(NL),TH_NCN(NL),
  * TH_NCOD(NXNP)
  COMMON /FRON3/ R1(NXNP),SK(NXNP),AA(25,25)
  COMMON /XNDVAR/ X(ND),Y(ND),U(ND),V(ND),P(ND),T(ND)
  COMMON /OLDVAR/ HOLD(ND),YOLD(ND),UOLD(ND),VOLD(ND),POLD(ND),
  * TOLD(ND)
  COMMON /SHPFCT/ PHI(9),PHIX(9),PHIY(9),PHIC(9),PHIE(9),PHIP(4)
  COMMON /BDYEL/ NBL(NL),NBO(NL),IQ,LB
  COMMON /NODCOO/ XE(9),YE(9),YE1(9)
  COMMON /PAR/ RE,FR,CA,ALPHA1,AMP,FREQ,XLDIM,WANU,BETA,NSTP1
  COMMON /TH_PAR/ DIFF,CONV_H,T_0,T_1,T_INF
  COMMON /PRES/ NNPRES(4),IL
  COMMON /RES1/ RF(NXNP)
  COMMON /XYWGT/ XWGHT(NG),XAGHT(NG),YAGHT(NG),YWGHT(NG)
  COMMON /SHPF1/ PHX1(9),PHY1(9)
  COMMON /JACB1/ XC1,XEDA1,YC1,YEDA1,Y11
C
  DIMENSION R(31,31)
  DIMENSION IU(9),IV(9),IP(4),IH(3),NNFRSF(3),IT(9)
  DIMENSION DX(3),DYY(3),DXY(3),DYX(3),DYTDH(3)
C
  DATA IT /1,2,3,4,5,6,7,8,9/
  DATA IU /1,4,6,9,11,13,15,18,20/
  DATA IV /2,5,7,10,12,14,16,19,21/
  DATA IP /3,8,17,22/
  DATA IH /23,24,25/
  DATA NNPRES /1,3,7,9/
  DATA NNFRSF /10,11,12/
C
  NGP = 9
  IQ = 9
  IL = 4
  EEU = 0.
  EEOLD = 0.
C
  XIM=1./2.
C
  C Initialize Jacobian ,R, and remember residual ,R1, is initialized in FRONT
C
  DO 101 I = 1, 31
    DO 101 J = 1, 31
      R(I,J) = 0.
  101 CONTINUE
C
  C Give global coordinates to the master element for isoparametric mapping
C
  DO 102 J = 1, IQ
    LN = IABS(NOP(NELL,J))
    XE(J) = X(LN)
    YE(J) = Y(LN)
    YE1(J) = YOLD(LN)
  102 CONTINUE
C
  C Implement steady or Crank-Nicholson transient
C
  IF (ICONT .LE. 1) THEN
    XIM = 1.
  ELSE
    XIM = 1./2.
  END IF
C
  C Assembly of R and R1
C
```

```

DO 103 K = 1, NGP
C   = GPX(K)
E   = GPY(K)
CALL TFUNC(C,E)
CALL DER(C,E)
TEVX = FEVX(T,NELL,EEU)
TEVY = FEVY(T,NELL,EEU)
TEV  = FEV(T,NELL,EEU)
UEV  = FEV(U,NELL,EEU)
VEV  = FEV(V,NELL,EEU)
C
WE   = GWEI(K)*Y1
WE1  = GWEI(K)
C
IF (ICONT .GE. 2) THEN
CALL DER1(C,E)
TEVOLD = FEV(TOLD,NELL,EEOLD)
TOVX   = FEVX1(TOLD,NELL,EEOLD)
TOVY   = FEVY1(TOLD,NELL,EEOLD)
UEVOLD = FEV(UOLD,NELL,EEU)
VEVOLD = FEV(VOLD,NELL,EEU)
YEV    = FEV(Y,NELL,EEU)
YEVOLD = FEV(YOLD,NELL,EEU)
DTDTT  = (TEV-TEVOLD)/TSTEP
DYDTT  = (YEV-YEVOLD)/TSTEP
DTDTP  = DTDTT-TEVY*DYDTT
ENDIF
C
C Compute -R1 (load term)
C
DO 104 KI = 1, IQ
IX = TH_NOPP(IABS(NOP(NELL,KI)))
R1(IX) = R1(IX) - XIM*WE*(DIFF*(PHIX(KI)*TEVX+PHIY(KI)*TEVY) +
* (UEV*TEVX+VEV*TEVY)*PHI(KI))
IF (ICONT .GE. 2)
*R1(IX) = R1(IX) - XIM*WE*(DIFF*(PHX1(KI)*TOVX+PHY1(KI)*TOVY) +
* (UEVOLD*TOVX+VEVOLD*TOVY)*PHI(KI))
IF (ICONT .GE. 2)
*R1(IX) = R1(IX) - WE*DTDTP*PHI(KI)
C
C Compute the derivatives of R1 wrt T
C
DO 105 KJ = 1, IQ
KKI = IT(KI)
KKJ = IT(KJ)
R(KKI,KKJ) = R(KKI,KKJ) + XIM*WE*(DIFF*(PHIX(KI)*PHIX(KJ) +
* PHIY(KI)*PHIY(KJ)) +
* (UEV*PHIX(KJ) +
* VEV*PHIY(KJ))*PHI(KI))
IF (ICONT .GE. 2)
*R(KKI,KKJ) = R(KKI,KKJ) + WE*(PHI(KJ)/TSTEP -
* PHIY(KJ)*DYDTT)*PHI(KI)
105 CONTINUE
C
104 CONTINUE
C
103 CONTINUE
C
C Free boundary condition at the outflow
C
IF (NBO(NELL) .EQ. 1) THEN
C
DO 108 K = 1, 3
C   = 1.
E   = GPT(K)
CALL TFUNC(C,E)
CALL DER(C,E)
TEVX = FEVX(T,NELL,EEU)
IF (ICONT .GE. 2) THEN
CALL DER1(C,E)
TOVX = FEVX1(TOLD,NELL,EEOLD)
ENDIF
C
WT   = GWE(K)*YEDA
C
C Add the appropriate contribution to -R1
C
DO 109 KI = 7, 9
IX = TH_NOPP(IABS(NOP(NELL,KI)))
R1(IX) = R1(IX) + XIM*WT*DIFF*PHI(KI)*TEVX
IF (ICONT .GE. 2)
*R1(IX) = R1(IX) + XIM*WT*DIFF*PHI(KI)*TOVX
C
C Computation of derivatives for volume integrals
C
DO 110 KJ = 1, IQ

```

```

KKI = IT(KI)
KKJ = IT(KJ)
R(KKI, KKJ) = R(KKI, KKJ) - XIM*WT*DIFF*PHI(KI)*PHIX(KJ)
110 CONTINUE
C
109 CONTINUE
C
108 CONTINUE
C
END IF
C
C Convection boundary condition along the free surface
C ATTENTION: CONV_H=Bi because of nondimensionalization
C T_INF=0 when Tair=To
C
IF (NBL(NELL), EQ. 1) THEN
C
DO 600 K = 1, 3
E = 1.
C = GPT(K)
CALL TFUNC(C,E)
CALL DER(C,E)
TEV = FEV(T,NELL,EEU)
IF (ICONT .GE. 2) THEN
CALL DER1(C,E)
TEVOLD = FEV(TOLD,NELL,EEU)
ENDIF
C
SQT2 = XC*XC+YC*YC
SQT = SQRT(SQT2)
SQT1 = SQRT(XC1*XC1+YC1*YC1)
WE = GWE(K)
C
DO 601 KI = 3, 9, 3
IX = TH_NOPP(IABS(NOP(NELL,KI)))
R1(IX) = R1(IX) - XIM*WE*PHI(KI)*CONV_H*(TEV-T_INF)*SQT
IF (ICONT .GE. 2)
*R1(IX) = R1(IX) - XIM*WE*PHI(KI)*CONV_H*(TEVOLD-T_INF)*SQT1
C
DO 601 KJ = 1, 9
KKI = IT(KI)
KKJ = IT(KJ)
R(KKI, KKJ) = R(KKI, KKJ) + XIM*WE*PHI(KI)*CONV_H*PHI(KJ)*SQT
601 CONTINUE
C
600 CONTINUE
C
END IF
C
C Tranfer the Jacobian to the Frontal solver
C
DO 172 I = 1, 25
DO 172 J = 1, 25
AA(J,I) = R(J,I)
172 CONTINUE
C
RETURN
END

```



ΠΑΝΕΠΙΣΤΗΜΙΟ
ΘΕΣΣΑΛΙΑΣ



004000074078